

ABSTRACT

COLLEGE, DAVID ALAN. Ultrafine-Grained Surface Layers on S7 Tool Steel via Electron Beam Irradiation and Cryogenic Freezing. (Under the direction of Dr. Yuntian Zhu).

Electron beam (e-beam) treatment of tool steel surfaces has been available for several decades as an approach to create hard surface layers which potentially increase the service life of tools. Irradiation pulses incident on a surface for only a few micro-seconds can be sufficient to induce melting of a surface layer which may be on the order of several microns in thickness. The much larger mass of the substrate is a very efficient heat sink resulting in cooling rates much more rapid than are normally found in industrial heat treatment processes. Ultrafine grain sizes result from the ultra-rapid cooling of the melt layer. Due to the Hall-Petch phenomena, a high hardness which improves wear resistance is predicted for the ultrafine-grained layer. This work yielded actual hardness gains of 9.9 to 36.1% on the surface of previously quenched and double-tempered S7 tool steel.

Despite the value of elevated hardness as a result of e-beam treatment, the dynamics of the rapid cooling leads to potentially detrimental residual tensile stresses. Implementation of the e-beam process has been limited in many applications by this accompanying residual tensile stress in the surface layer, which may lead to premature fracture. This work provides an investigation into the treatment of S7 tool steel with both e-beaming to increase hardness and cryogenic freezing after e-beaming to reduce the residual tensile stress. The e-beamed surface layer was found to contain over 4 times the amount of retained austenite found in an unbeamed specimen. The cryogenic treatment is believed to convert retained austenite into martensite and experience a corresponding volume expansion. The cryogenic treatment reduced the peak tensile residual stress by 28%, which makes it a promising method to expand the applications of e-beamed tool steel.

© Copyright 2018 David Alan College

All Rights Reserved

Ultrafine-Grained Surface Layers on S7 Tool Steel via Electron Beam Irradiation and
Cryogenic Freezing.

by
David Alan College

A dissertation submitted to the Graduate Faculty of
North Carolina State University
in partial fulfillment of the
requirements for the degree of
Doctor of Philosophy

Materials Science and Engineering

Raleigh, North Carolina
2018

APPROVED BY:

Yuntian Zhu
Committee Chair

Ronald Scattergood

Carl Koch

Korukonda Murty

DEDICATION

To my family: Sharon, Jeffrey, Becca, Kristen, and Daniel. You bring me great joy!

To my parents. Thank you for the love and support.

To the One who designed my gifts and being. “Whatever you do, work at it wholeheartedly as though you were doing it for the Lord and not merely for people.” Colossians 3:23 (ISV)

BIOGRAPHY

I was born in Lebanon, PA and raised by my parents, Barry and Mary College, along with two younger siblings, Dennis and Kathy, in predominately rural south-central Pennsylvania. Farms, woods, and mountains all became comfortable environments for me. I also found in myself a natural curiosity about how man-made things worked, how they were put together, and how they could be fixed. Books and learning were usually enjoyable for me. I graduated from Annville-Cleona High School as Co-Valedictorian in the class of 1983. Besides academics, I stayed very active in my school years with church activities, Boy Scouts, running with the track and cross-country teams, playing trombone in school bands, hunting, fishing, and following Phillies baseball.

I entered Bucknell University in Lewisburg, PA during the fall of 1983 to pursue a Mechanical Engineering degree. During my time there I was fortunate to experience summer internships at General Electric, The Small Business Development Center at Bucknell, and Combustion Engineering. While I was at Bucknell, I also met my future wife, Sharon. After 4 years of study I was able to graduate Summa Cum Laude with a BSME degree.

Following graduation, I began a career journey with AMP Incorporated, now TE Connectivity, as a Machine Development Engineer. Most of my work with the company has been focused on developing application tools and equipment for the assembly of electrical and electronic harnesses and devices. I have received 18 patents for this work. I also earned my Pennsylvania Professional Engineer License several years into my career. After thirty-plus years of experience with the company, I currently serve as a Principal Research and Development Engineer.

After a few years of mechanical design experience, I began to see how material selection and treatment can be used to solve mechanical problems and improve performance of mechanical parts. A great synergy exists between the two fields. I gradually began informally extending my materials education on the job. After many years, as my 3 children – Jeffrey, Kristen, and Daniel – began achieving self-reliance and starting their own college experiences, I felt perhaps I now had the time to formalize my materials training. I enrolled in the distance education program at North Carolina State to take a few courses. Soon, a few courses became the pursuit of a master's degree in Materials Science and Engineering, and then a launching of discussions about how a predominately distance learning PhD could look. Dr. Zhu enthusiastically encouraged the possibility and with my employer's help and blessing I jumped in with both feet.

Outside of my career and studies, you will find me pursuing a few other interests. I enjoy spending time with my family and doing a little gardening. I am still active in church activities including leading the church orchestra. Recently, as I neared the end of my PhD journey, my studies and experience opened the door to serve as a part-time adjunct instructor for the basic Materials Engineering class at Messiah College near Mechanicsburg, PA. Teaching and building into young lives in the classroom and orchestra room has been very rewarding.

ACKNOWLEDGMENTS

Portions of this work were published on April 11, 2018 in Materials Science and Engineering A.[1]

I would like to acknowledge TE Connectivity for support and all funding for this work. I am grateful for the technical advice and support from Dr. Aleksander Angelov who served as a Technical Consultant on my advisory committee. Dr. Rodney Martens, Dr. Drew Athans, Dr. Martin Bayes, and Dr. Suvrat Bhargava from TE Connectivity were also appreciated as technical advisors and colleagues. The support provided by Neil Deming, Matt Houser, David Weaver, Keith Nicholas, Susan Wallace and the entire Application Tooling group within TE is also greatly appreciated.

I enthusiastically thank my academic advisor, Dr. Yuntian Zhu of North Carolina State University, for his advice and encouragement as well as his flexibility in working with an unusual off-campus student-advisor association. Additionally, my advisory committee, Dr. Carl Koch, Dr. Ron Scattergood, and Dr. Korukonda Murty are also thanked for their time, discussions, and advice.

I am grateful for the time invested by Natalie Wheeler who was my primary proofreader and provided many insightful editing suggestions. Additional editing help was provided by Sharon College and Kristen College.

The XRD work for determination of retained austenite was carried out by TEC, 10737 Lexington Dr., Knoxville, TN which is accredited by the American Association for Laboratory Accreditation.

The XRD work for determination of residual stress was carried out by Lambda Research 5521 Fair Lane, Cincinnati, OH which is accredited by the American Association for Laboratory Accreditation.

TABLE OF CONTENTS

LIST OF TABLES	ix
LIST OF FIGURES	x
1. INTRODUCTION	1
1.1. Motivation for Investigation.....	1
1.2. Scope of Investigation	1
2. BACKGROUND AND LITERATURE REVIEW	3
2.1. Irradiation of Surfaces.....	3
2.2. E-beaming Development.....	8
2.3. Interaction of an Electron Beam with a Ferrous Substrate.....	10
2.4. Ultrafine and Nanocrystalline Grains.....	14
2.5. Consideration of Amorphous Structure.....	21
2.6. Residual Stress	22
3. EXPERIMENTAL PROCEDURES	28
3.1. Tool Steel Specimens.....	28
3.2. Electropolishing	29
3.3. E-beaming Device and Process	32
3.4. Cryogenic Treatment.....	33
3.5. X-Ray Diffraction(XRD)	34
3.5.1 General Diffraction Principles.....	34
3.5.2 X-Ray Diffraction for Phase Identification.....	37
3.5.3 X-Ray Diffraction for Residual Stress Determination.....	40
3.6. Nanoindentation	43
3.7. Grain Size	50
3.8. Coefficient of Friction	52
4. RESULTS AND DISCUSSION	54
4.1. XRD Analysis for Retained Austenite	54
4.2. XRD Analysis for Residual Stress	56
4.3. Nanohardness	58
4.4. Grain Size.....	62

4.5. Coefficient of Friction	64
5. POTENTIAL FOR FUTURE WORK	68
6. CONCLUSIONS	69
7. REFERENCES.....	70

LIST OF TABLES

Table 1. Definitions for grain size used in this work.....	14
Table 2. General classification of hardness testing methods.....	44
Table 3. Surface nanohardness with various treatments.....	59
Table 4. Dynamic coefficient of friction test results: tungsten carbide ball on variously treated S7 steel surfaces	65

LIST OF FIGURES

Figure 1. Schematic of the typical energy absorption profile of laser and electron beam heating.....	5
Figure 2. Schematic of nucleation and formation of surface melt layer from e-beam bombardment.....	6
Figure 3. Solidification of layer melted by beaming	7
Figure 4. Schematic diagram of a wide-aperture electron beam apparatus utilizing plasma.	10
Figure 5. Iron - Iron Carbide (Fe - Fe ₃ C) Equilibrium Phase Diagram	12
Figure 6. Schematic of dislocation pile-up at a grain boundary	16
Figure 7. Schematic of deformation theory according to Cottrell.	17
Figure 8. Illustration of core and mantle model of grain boundary strengthening	18
Figure 9. Strengthening effect for iron with reducing grain size.	19
Figure 10. Hall-Petch effect for electrodeposited Ni-Fe.....	20
Figure 11. Depiction of plane stress in a surface layer	24
Figure 12. Schematic of stress effect on differently oriented lattices	25
Figure 13. Schematic of expected stress states in e-beamed layers during melting and after conduction cooling to the substrate heat sin	26
Figure 14. Stress pattern proposed for instance when solidification front starts on surface .	27
Figure 15. Specimens ready for e-beam treatment	28
Figure 16. Schematic of surface finish improvement over time during electropolishing	29
Figure 17. Schematic of typical electropolishing process	30
Figure 18. General current to voltage relationship for electrochemical treatments to metal surfaces.....	31
Figure 19. Masking of specimen during electropolishing	32
Figure 20. The Sodick PF32B e-beam device used for surface treatment.....	33
Figure 21. Diffraction of X-rays by a crystal lattice.....	35
Figure 22. Schematic of basic X-ray diffraction device	36

Figure 23. X-ray diffraction scan of a single-phase solid(NaCl) illustrating intensity peaks for different plane systems	37
Figure 24. XRD results of medium carbon, low alloy steel at 2 stages of heat treatment	38
Figure 25. Sample mounted in the XRD equipment for retained austenite determination	39
Figure 26. Changes to XRD diffraction peak under strain	40
Figure 27. Schematic illustration of XRD Ψ rotations and diffraction peak movement under stress	42
Figure 28. Example of linear d vs. $\sin^2\Psi$ plot used to determine m	42
Figure 29. Illustration of pile-up and sink-in phenomena as a result of indentation	45
Figure 30. Schematic of load and unload data curve for nanoindentation.....	46
Figure 31. AFM images of a Berkovich-type tip.....	47
Figure 32. Illustration of malformed 4-face indenter.....	48
Figure 33. Representative load curves for a set of 50mN indentations with Berkovich indenter	49
Figure 34. AFM scan of several representative nanoindentations in a specimen	50
Figure 35. Specimen clamped in AFM unit for scanning of grain size and nanoindentation size	51
Figure 36. Schematic of tribological testing equipment for determination of coefficient of friction.....	52
Figure 37. View of tungsten carbide ball in holder and engaging test sample during friction coefficient test	53
Figure 38. Retained austenite at various depths in e-beamed layer	55
Figure 39. Residual stress in e-beamed samples as determined with XRD analysis	57
Figure 40. Nanohardness vs. depth after 1 e-beam pulse	59
Figure 41. Nanohardness vs. depth after 8 e-beam pulses.....	60
Figure 42. Nanohardness vs. depth after 1 e-beam pulse plus cryogenic treatment	60
Figure 43. Nanohardness vs. depth after 8 e-beam pulses plus cryogenic treatment	61
Figure 44. Nanohardness profile comparison of various e-beamed surface treatments	62

Figure 45. AFM of sample with nanoindentation after electropolishing to 2 μm depth 63

Figure 46. Coefficient of friction test for WC ball and unbeamed control sample 65

Figure 47. Coefficient of friction test for WC ball and sample e-beamed with 1 pulse 66

Figure 48. Coefficient of friction test for WC ball and sample e-beamed with 8 pulses..... 66

Figure 49. Coefficient of friction test for WC ball and sample e-beamed with 1 pulse
and cryogenically treated..... 67

Figure 50. Coefficient of friction test for WC ball and sample e-beamed with 8 pulses
and cryogenically treated..... 67

1. INTRODUCTION

1.1. Motivation for Investigation

Various methods of forming materials into useful products rely on punches, dies, shears, and other tools produced from hardened tool steel. This is particularly true in the electrical and electronics industries in which this author is immersed. Nonferrous metals, and sometimes soft ferrous metals, are stamped and formed into electrically conducting terminals and then crimped onto wire ends. The tools required to do these operations experience wear despite the relative hardness and strength of tool steel in comparison to the materials being worked. New tool materials or surface treatments which help the tool withstand wear are worth investigating. Tool longevity pays dividends in tool costs and reduced down-time and makes production planning more certain.

1.2. Scope of Investigation

Irradiation of tool steel surfaces is of interest as a method of improving wear on forming tools. Specifically, electron beam (e-beam) surface treatment of ASTM A681 type S7 tool steel (S7) will be studied. A literature search did not uncover any specific studies on e-beam treatment of the S7 alloy. The investigation of e-beaming of S7 will look at the hardness profile created, and the surface coefficient of friction created. The grain size in the e-beamed layer will be investigated to explain the expected hardening effect. A significant problem to address with the use of e-beamed surface layers is the creation of residual tensile stresses[2][3] which limits the suitable applications for the technology. Residual tensile

stress abatement via cryogenic freezing is proposed and will be studied. No published studies have been found which utilize cryogenic temperatures (or any other means) for reducing residual stress in e-beamed steel surface layers. X-ray diffraction (XRD) techniques will be used to evaluate residual stress and the phases present in the layer.

2. BACKGROUND AND LITERATURE REVIEW

2.1. Irradiation of Surfaces

Irradiation sources such as lasers, e-beams, and ion beams can produce very intense, localized energy for treating and modifying the surface of materials. Beam treating of surfaces was initiated with lasers for semiconductor processing in the 1960's.[4] Exploration of the technique in subsequent years expanded to include e-beams and ion beams for the treatment of a wide array of materials.[4] The interaction of highly energetic incident photons, electrons, or ions with the electronic structure of the atoms near the treated material's surface will create intense heat.[5] This heat derives from electrons jumping to higher energy bands and then transferring energy to phonons as they return to a lower energy band.[6] Photon beams can only excite conduction and valance band electrons, whereas high-energy electron and ion beams can also interact with electrons in core shells.[6] The collision of beam particles with the substrate atoms' nuclei is elastic and inconsequential in the case of photons and electrons [6] but significant for ions.[7] Depending on the particle energy, beam bombardment on a substrate also creates shock waves which may affect microstructure slightly below the melted and quenched layer.[2][8][9] One explanation is that repeated shock waves drive carbon diffusion in martensite to form very small dispersed Fe₃C precipitates.[8] The generated particle stopping heat and shock waves can be investigated as mechanisms to affect microstructure in a ferrous surface layer for hardening it to increase wear resistance.

The essential aspect of each of the several beaming processes is that high energy particles stream toward, and collide with, a substrate surface over a prescribed duration. When surface treatment is the goal, the burst of colliding particles is usually very short. Basic differences among the beaming processes also exist. The e-beam and ion beam methods generally require a vacuum. The creation of a vacuum makes a process more expensive and time consuming. Some e-beaming apparatuses have been developed which utilize plasma to conduct the electrons, a process which still requires a vacuum to be created as a preliminary step. Laser surface treating processes must overcome the complication that photons may be easily reflected by metals. Careful consideration must be made to select the wavelength so that it is absorbed by the substrate being treated. In many cases when metallic substrates are laser treated, coatings which facilitate the efficient absorption of the beam must first be applied to the surface.[5][10]

The heat produced by electronic and possibly nuclear stopping of particle beams can accumulate very rapidly. Heating rates as high as 10^6 to 10^{10} °C/s are sometimes attained[4][5], although more modest rates can also be practical and effective.[10] Commonly, enough heat is created to melt a surface layer. Figure 1 schematically shows general energy absorption profiles for short bursts of both a typical laser beam and a typical e-beam incident on a substrate. Individual applications and equipment will cause results to vary considerably. Owing to their mass, beamed electrons with sufficient speed can carry deeper into the substrate than photons and often impart the highest energy at a depth slightly below the surface.[11] Ion beams, not shown in Figure 1, have the potential to penetrate even more deeply than electrons due to even higher mass.

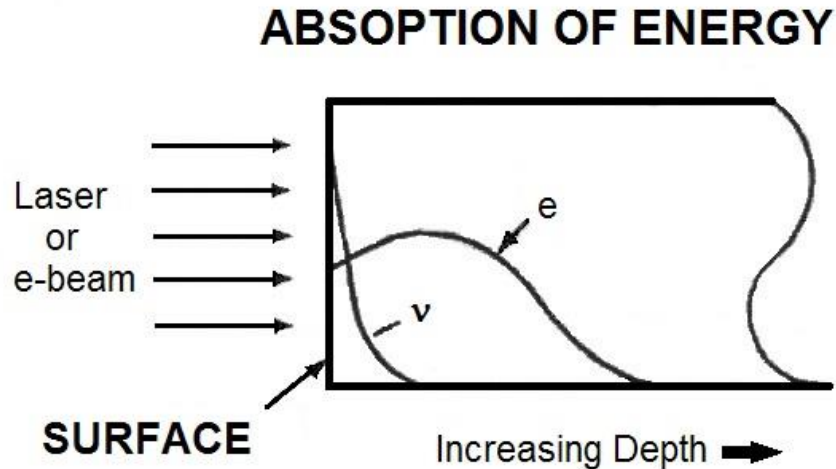


Figure 1. Schematic of the typical energy absorption profile of laser and electron beam heating (e = electron energy, v = photon energy) – adapted from [11]

The depth of greatest energy absorption for an e-beam or an ion beam will be the depth at which melting nucleates, as shown in Figure 2a. Next, melt fronts will proceed very rapidly in both directions from the starting depth as shown in Figure 2b. One melt front will quickly reach the surface and the other will penetrate to a depth determined by overall energy intensity and duration. Beyond the melt, a heat affected zone will exist as shown in Figure 2c. The heat affected zone did not receive enough heat to cause melting, however the significant heat that was received here likely enables diffusion within the solid to make microstructural and phase changes. Proskurovsky et al., have found that practical durations for beam irradiation to achieve a fully melted layer are only on the order of one or several microseconds.[12][13]

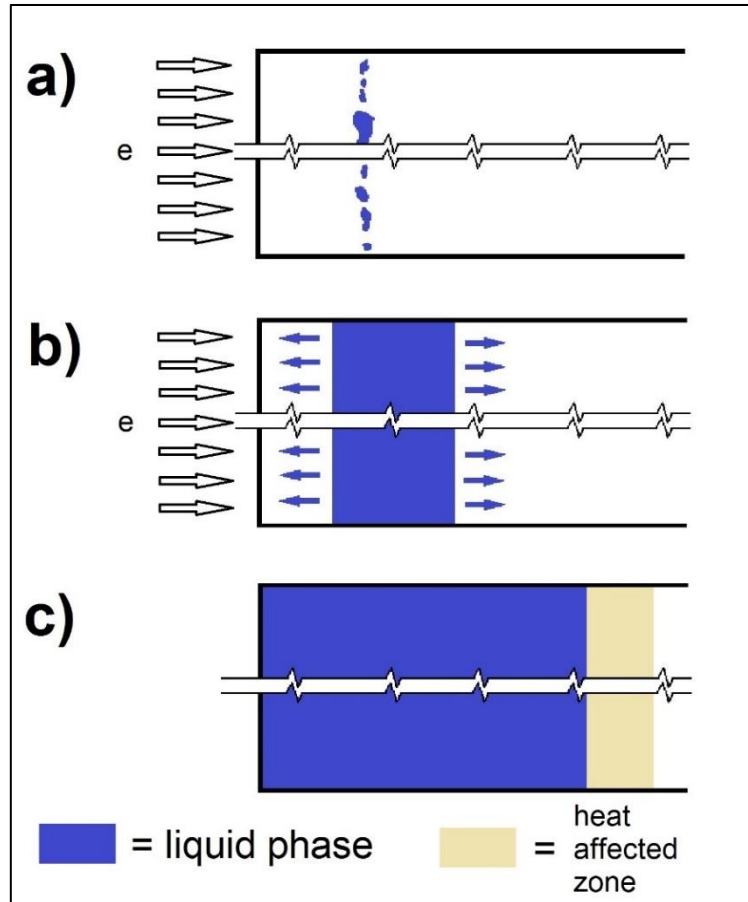


Figure 2. Schematic of nucleation and formation of surface melt layer from e-beam bombardment.

Cut lines indicate irradiated surface is much wider than the depth of penetration.

a) nucleation b) melt fronts moving c) final melted depth and heat affected zone after termination of beam

When the radiation is terminated, the melted layer will self-quench with no cooling media needed because the substrate is a comparatively massive thermal sink.[4][14] The substrate will conduct heat away from the melt with a very steep temperature gradient, and a solidification front will proceed very rapidly back toward the surface as shown in Figure 3b. When the mass of the substrate heat sink is very large compared to the mass of the melted layer, conductive cooling rates may range over similar magnitudes to the heating rates.[5][8][12] Evaporation of material from the melt will provide additional cooling to the

surface of the melted liquid.[15][16] The partial vacuum atmospheres common for e-beam processes will accelerate evaporative cooling. Radiative heat loss, and in rare cases convective heat loss, will also provide a minor contribution to cooling from the surface.[15] Due to evaporation, radiation, and possibly convection, a solidification front may also start from the surface and proceed into the melt until it meets the solidification front proceeding from the cold substrate. Figure 3c illustrates schematically the start of a surface solidification front if surface cooling is very high.

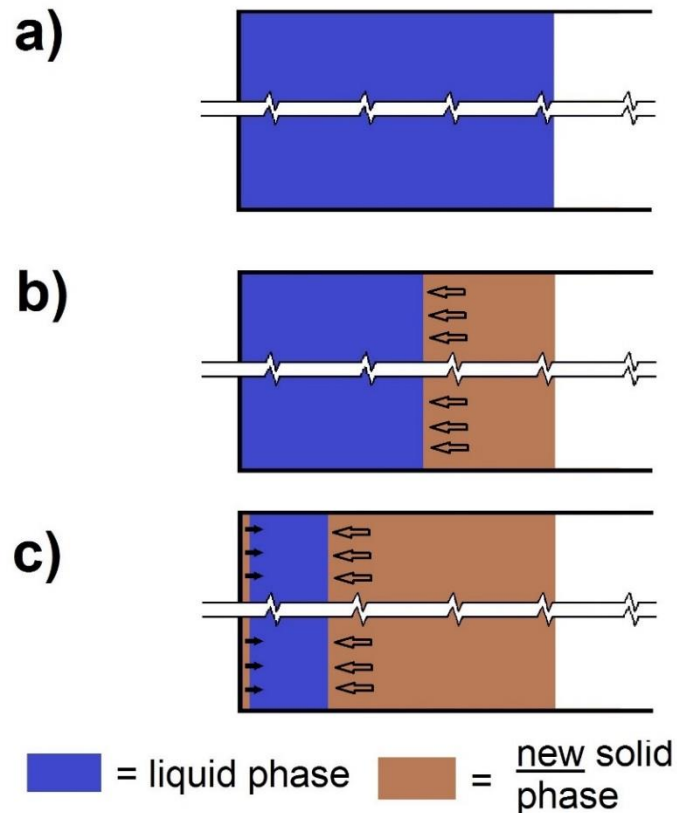


Figure 3. Solidification of layer melted by beaming.

Cut lines indicate irradiated surface is much wider than the depth of penetration.

a) completion of melting b) conduction solidification front moving c) potential surface solidification front forming

2.2. E-beaming Development

The use of e-beam treatments to harden the working surface of numerous alloy and tool steels has been studied by many investigators under various e-beam processing conditions.[3], [17]–[33]. Rotshtein asserts that advantages for choosing electron beam sources include the availability of wide apertures, reliability, electrical efficiency, and X-ray safety,[34] as well as the ability to achieve a broad range of incident energy levels.[8] The research being undertaken in this work will utilize a wide-aperture, pulsed e-beam source to harness these advantages.

Electron beams can be efficiently created in a vacuum or in a plasma. Some early investigations into treating metallic surfaces were done with direct acting e-beams generated in a vacuum and focused to form a microdot on the treated surface. Highly focused beams were familiar and available to science and industry from their use in cutting and welding operations. Since the beam incidence was only a microdot, a grid of many repeated exposures was required to cover an appreciable area.[22][35] Other researchers realized that a pulsed, wide-aperture beam would be useful and convenient in many material surface treatment situations.[12][36] Ozur et al. defines a wide-aperture beam as having $>10 \text{ cm}^2$ of area coverage.[37] Proskurovsky et al. showed that electron beams generated in vacuum are subject to discontinuities in beam density, and that the use of plasma as a conductor greatly improves beam homogeneity.[12][38] The combination of a wide aperture, a plasma conductor and a pulsed exposure represent the current state-of-the-art for e-beam surface treatment.

Figure 4 shows a general schematic of a wide-aperture plasma-based electron beam apparatus. An e-beam device of this type was used for the current research. In operation, a sample is affixed to the collector, shown as item 3 in Figure 4. After closure and sealing of the chamber case, a vacuum is created in the chamber. Then a small volume of plasma-forming gas, in many cases argon, is injected into the chamber. Ozur et al. indicate that a particle density of 10^{11} to 10^{14} cm^{-3} for the plasma-forming gas is effective.[37] The pressure of the plasma-forming gas at this density is still well below atmospheric pressure. For instance, Tang et al. used an argon pressure of 3×10^{-2} Pa for their work with M50 tool steel.[19] Various methods of generating plasma from a gas exist, including arc generation, auxiliary hot-cathode guns, and high-current reflected discharge.[37] Voltage applied at the anode and cathode separates plasmas of opposite charge into a double layer, as shown by labels 5 and 6 in Figure 4.[12] Due to the excellent conductivity of the plasma, the plasma clouds take the voltage of the adjacent cathode or anode.[12] A final pulse of accelerating voltage applied at the cathode causes electrons to explosively jump the gap between the cathode plasma and the anode plasma.[12] Electron flow proceeds toward the anode and ion current flows in the opposite direction.[37] The anode plasma can efficiently transfer up to 90% of the electron flow through the anode to the collector.[12] Some shaping of the electron beam can be accomplished with magnetic fields created by solenoid coils located around the device's case.[12][37]

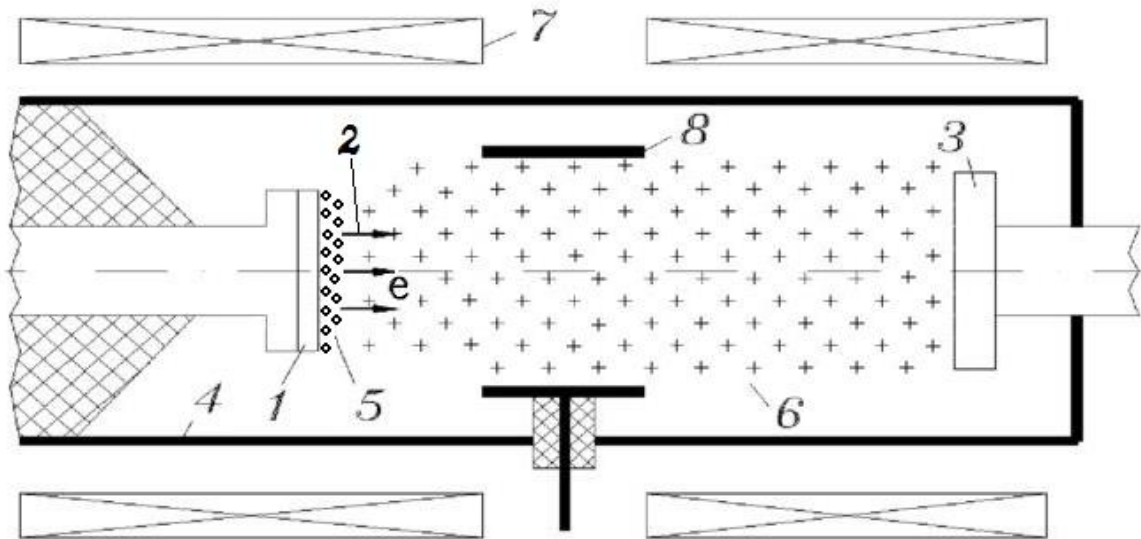


Figure 4. Schematic diagram of a wide-aperture electron beam apparatus utilizing plasma.

1: explosive emission cathode; 2: electron flow direction; 3: collector; 4: chamber case; 5: cathode plasma; 6: anode plasma; 7: solenoid coils; 8: anode -adapted from [37]

2.3. Interaction of an Electron Beam with a Ferrous Substrate

E-beams can produce very intense, localized energy for treating and modifying the surface of materials. An e-beam surface treatment often results in complete melting on the surface. In the case of ferrous surfaces such as S7, the required incident energy to create melting is about 2.5 J/cm^2 [8]. Dynamic re-solidification follows melting. The very rapid melting and cooling rates of the e-beam treatments can be used to tailor the resulting microstructure via the introduction of crystal defects and non-equilibrium structures.

In the case of a predominantly ferrous substrate, four solid phases of iron are germane to the discussion of microstructure. These solid phases are often given the short identifications of α , α' , γ , and δ . The equilibrium crystalline phase for iron at room temperature is ferrite, which is often labeled as α on an iron - iron carbide phase diagram such as Figure 5. Ferrite

has a body-centered cubic (BCC) crystalline structure. Carbides often also play a role in iron alloy microstructures because of the very low solubility of carbon in ferrite. The most common carbide is Fe_3C also known as iron carbide or cementite. For plain carbon steels, Fe_3C is an equilibrium constituent along with ferrite if carbon concentration is greater than just 0.022 weight percent. Under significant heating – at least 727°C for plain steel as shown in Figure 5 - face-centered cubic (FCC) austenite, the γ phase of iron, will form from the ferrite and cementite present. The carbon from the cementite will go into solution at interstitial sites in the austenite. Occasionally, the surface beaming process on ferrous alloys is varied so that the substrate heats to the point of transforming into austenite but does not reach melting.[22] With continued heating, γ iron with low carbon content will reform in a BCC arrangement identified as δ phase before reaching melting temperatures. As can be seen from Figure 5, higher carbon steels (with C wt % > .5) will melt without forming delta phase. The addition of alloying elements may skew the specific temperatures and concentrations on the basic phase diagram, and also enable the possibility of other carbides being formed.

In tool steels, many properties are affected by the presence of various carbides within the microstructure. Depending upon how and when they were formed, the carbides present before e-beaming may be along grain boundaries or precipitated within grains.[20] The carbides likely absorb beam energy at different rates than the steel substrate and also have different melting temperatures than the steel substrate. Sometimes the rapid absorption of heat by carbides can cause eruptions from the surface which may not completely heal without additional melt sequences.[23][28][30][39] Many experiments have shown that with

repeated e-beam pulses, the carbides can be completely dissolved into the melted layer.[20][3] High quench rates probably do not allow for re-precipitation of carbides. With each melt sequence it is estimated that any released alloying elements from the carbides can diffuse on the order of 100 nm.[33] With a large number of melt sequences, a homogenous layer containing the elements from the fully dissolved carbides will form a homogenous steel alloy of a different composition than the steel substrate which surrounds the carbides in the unmelted substrate.[19]

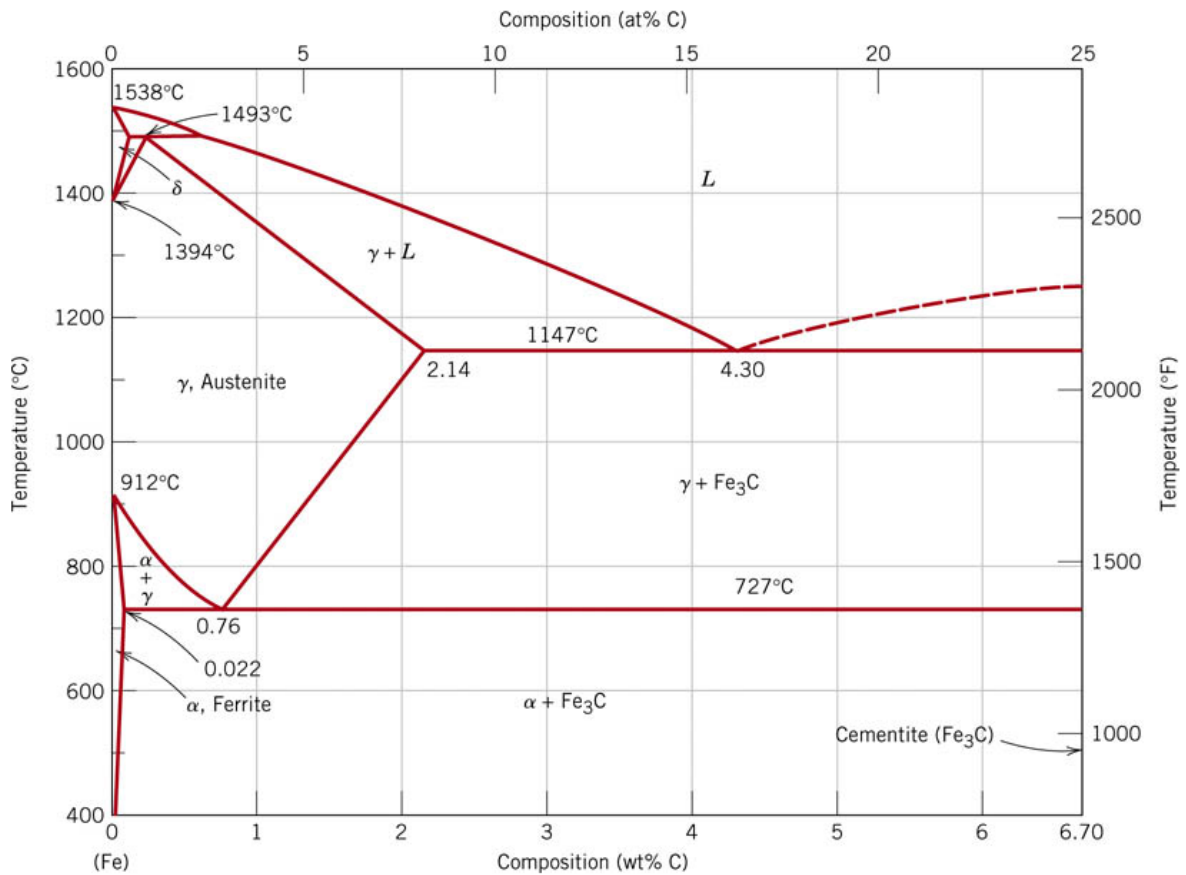


Figure 5. Iron - Iron Carbide (Fe - Fe₃C) Equilibrium Phase Diagram [40]

During cooling of low carbon melted steel, the alloy will pass through delta phase before its formation of austenite. Higher carbon alloys will nucleate austenite directly. When very rapid quenching of austenite occurs, austenite usually transforms into martensite which is a body-centered tetragonal structure (BCT) often identified as alpha prime phase (α'). Martensite does not show up on the iron - iron carbide equilibrium phase diagram because it is metastable. There is an activation energy which generally prevents it from changing to the lower-energy phases of ferrite and cementite. Metastable austenite may also be retained in the microstructure during rapid cooling. Although austenite is on the equilibrium phase diagram, its existence at low temperatures is not a low-energy condition for plain and low-alloy steels.

It is important to note that due to the very small melt thickness and the very short time durations, process variations can result in significant changes to melt kinetics and thus microstructure. Various researchers working with different steels and different beam parameters have reported contrasting conclusions about the phases created in the e-beamed layer. In some studies, for example Ivanov et al. [17], both austenite and martensite were found. Zou et al. proposed that dispersed alloy elements from the melted carbides contributed to stabilization of nearly pure austenite in D2 tool steel which was e-beamed 25 times.[28] Rotshtein cited evidence that very thin melt layers would not support the creation of martensite.[8] Zhang, et al, found some BCC phase mixed with martensite and austenite in e-beamed H13 tool steel. They proposed that the BCC content was retained δ phase.

2.4. Ultrafine and Nanocrystalline Grains

The creation of unusually small grain sizes is typically a primary goal of attempts to harden surfaces of normal, coarse grain (CG) metals via irradiation. According to Meyers and Chawla, CG metals from conventional industrial processes typically have grain sizes in the range of 10 - 100 μm . [41] This study aims to produce grains several orders of magnitude smaller than CG. For this discussion, nanocrystalline (NC) grains will be considered to have average size under 100 nm which follows Cavaliere [42], Hanlon [43], and others.

Occasionally, other writers such as Meyers et al. [44] have used 250 nm or another value as the cutoff for the NC regime. The definition for ultrafine (UF) grain size will also follow Cavaliere. [42] Table 1 lists the grain size definitions used for this discussion. For reasons to be explored next, the UF and NC grain sizes are desirable for getting appreciable surface hardness gains compared to CG metals.

Table 1. Definitions for grain size used in this work

Grain Size Class	Size Range	Comments
Coarse Grain (CG)	10 μm – 100 μm	Size developed from normal manufacturing processes.
Fine Grain	1 μm – 10 μm	
Ultrafine (UF) Grain	100 nm – 1 μm	
Nanocrystalline (NC)	10 nm – 100 nm	

When a melted surface on a common tool steel is undercooled to a temperature below the liquidus, austenite grains will nucleate in the liquid. The extremely rapid cooling rates after e-beam termination result in extremely undercooled conditions and the generation of

many more nucleation events than would occur with a normal industrial solidification process such as casting. With plentiful nucleation events occurring, the grains cannot grow far until they encounter other growing grains, which significantly limits average grain size. In normal circumstances, as cooling continues below the martensite start temperature, martensite laths or plates nucleate within the prior austenite grains. In addition, it has been shown that for some steel chemistries, faster cooling rates also increase the martensite start temperature, encouraging nucleation of more martensite laths or plates within the prior austenite grain.[45] As a consequence, the martensitic structure will be finer. There may be a competing factor in that smaller austenite grains make it more difficult for the shearing action of the lattice to occur in the martensite transformation. Overall, though, the more rapid the cooling, the smaller the grain and sub-grain size.

According to the well-known Hall-Petch relationship, grain boundaries and sub-grain boundaries act to strengthen and hardened metals.[46][47] The classic theory on the cause of the Hall-Petch relationship presumes that dislocations are generated inside the grain due to stress at a Frank-Read source and move under stress until they pile up at grain boundaries. Figure 6 illustrates dislocation pile-up. A higher stress is required at the boundary to activate a slip system in the adjacent grain and cause deformation to continue.[44][48] Thus, grain boundaries are crystal defects which resist dislocation movement and strengthen the material. As grain sizes get much smaller, the likelihood of abundant dislocations existing within the grain and the likelihood of accumulating enough dislocation pile-up to initiate adjacent grain slip is small, resulting in higher yield strength.[48] The Hall-Petch equation relates yield strength, σ_y , to grain size, d , according to the following relation:

$$\sigma_y = \sigma_0 + kd^{-1/2}.$$

For this equation, σ_0 , is the friction stress required to move a dislocation through a perfect material lattice, and k is a constant which will vary with material. Sometimes, the original Hall-Petch form is modified to a general exponent to better fit data collected:

$$\sigma_y = \sigma_0 + kd^{-n}.$$

The variable n in the exponent is generally found to be such that $0.3 \leq n \leq 0.7$. [44]

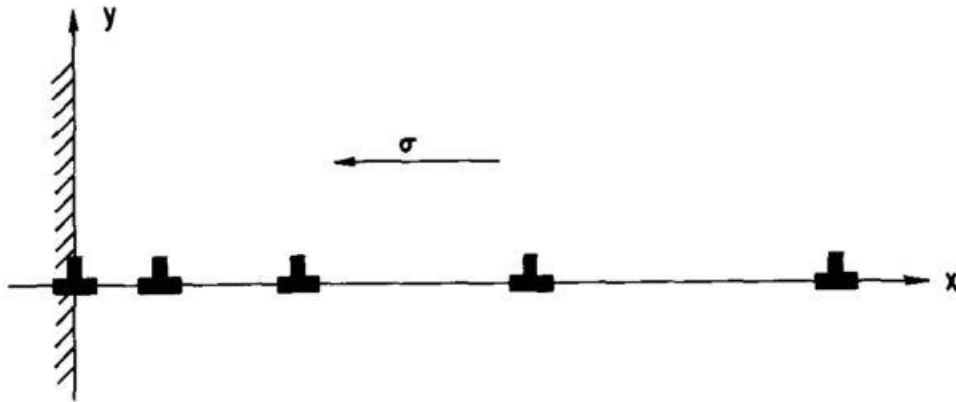


Figure 6. Schematic of dislocation pile-up at a grain boundary [49]

A few years after the Hall and Petch papers were published, Cottrell proposed a variation on the theory. Cottrell posited that dislocations wouldn't really move through a boundary. Instead, he modeled a dislocation pileup as a crack and calculated the stress the crack would transfer to the neighboring grain. [50] He proposed that Frank-Read sources within the neighboring grain and at close proximity to the boundary, would generate new dislocations,

and thus deformation, from the stress of the pileup against the grain boundary. The Cottrell method still results in an equation of the Hall-Petch form.[41]

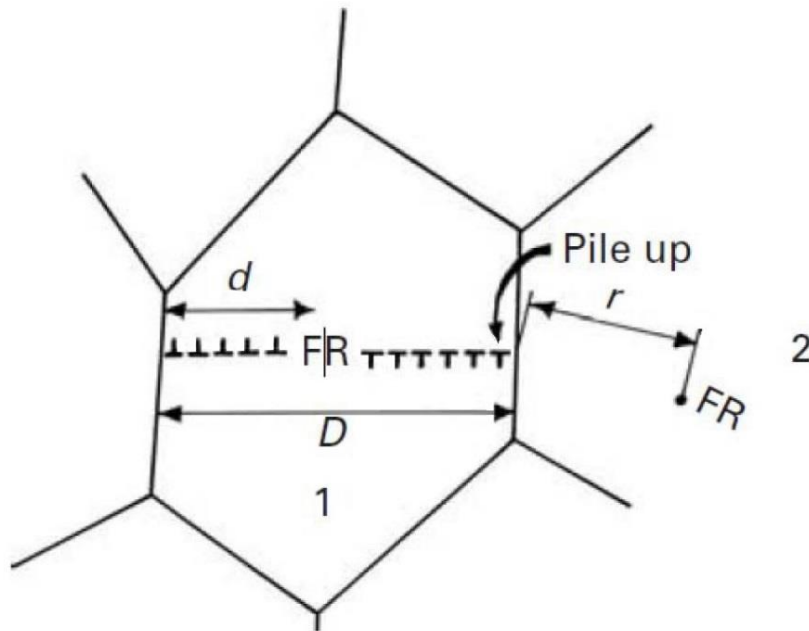


Figure 7. Schematic of deformation theory according to Cottrell. Stress from pileup in one grain activates Frank-Read sources in neighboring grains.[41]

However, at a critical grain size, the dislocation pile-up models will no longer work.[44] Very small grains will not have enough dislocations and dislocation sources. Alternate models of grain size strengthening were needed and have been proposed. Li and Chou proposed that grain boundaries themselves could be the source of dislocations.[51] Fleck et al. [52], building on the work of Ashby[49]and Li[51], proposed that grain boundaries stored both random and geometrically necessary dislocations which hardened the grain boundary.

Meyers and Ashworth [53] developed a model that has come to be termed “core and mantle” which is depicted in Figure 8. They propose that grain boundaries act as work

hardened reinforcements and that the interior of the grain is softer. Further, they propose that a high initial microstress is needed to create a microyield at the harder grain boundary to initiate progressive macroyielding through the grain. The core and mantle model results in a yield strength relationship using a “law of mixtures” of the flow stress inside the core or bulk of the grain, σ_{fB} , and the flow stress in the mantle or grain boundary, σ_{fGB} . [53] With the use of A_B for the areal fraction of the bulk within the grain, and A_{GB} for the areal fraction of the grain boundary, the following expression can be formed:

$$\sigma_y = A_B \sigma_{fB} + A_{GB} \sigma_{fGB}.$$

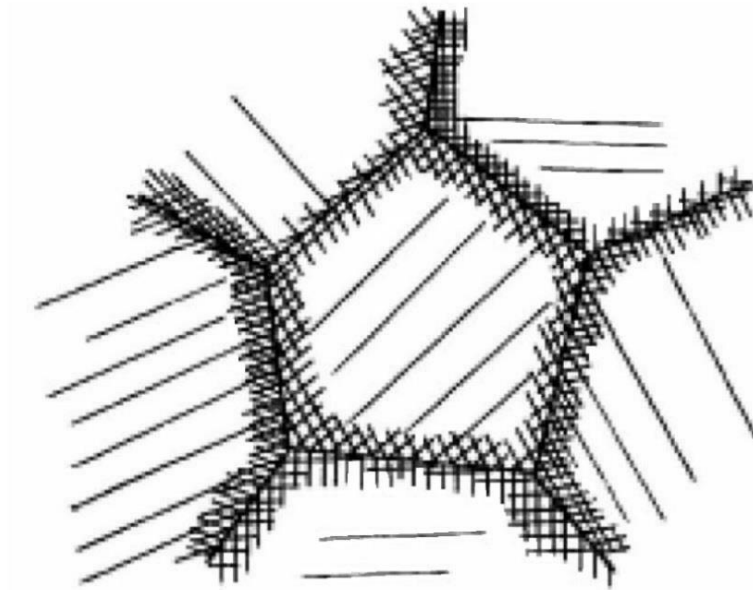


Figure 8. Illustration of core and mantle model of grain boundary strengthening [44]

With some geometric assumptions and mathematical analysis, Meyers and Ashworth developed their equation into the following form [53]:

$$\sigma_y = \sigma_{fB} + k_1(\sigma_{fGB} - \sigma_{fB})d^{-1/2} - k_2(\sigma_{fGB} - \sigma_{fB})d^{-1}.$$

If the last term is ignored, the equation is in the general form of the Hall-Petch equation. For CG and fine grain sizes as defined in Table 1, the equation generally does follow the Hall-Petch result as the last term is small.[48] However, the rate of hardness increase will be reduced in the UF and NC grain sizes as the last term begins to be significant. Figure 9 shows experimental results that confirm this trend.

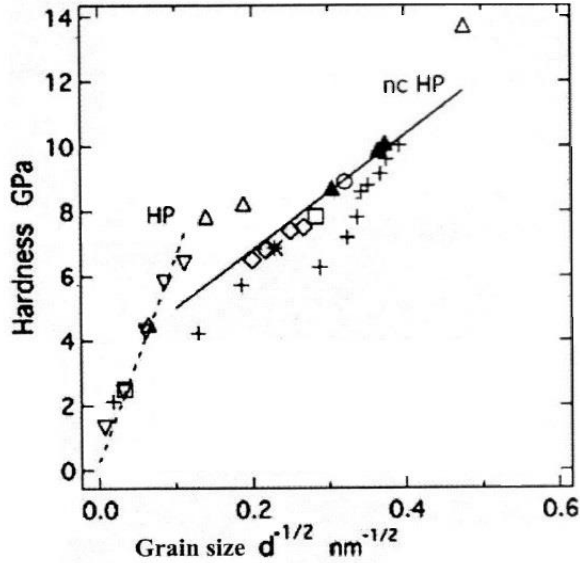


Figure 9. Strengthening effect for iron with reducing grain size. The rate of Hall-Petch strengthening in the CG regime is greater than the rate in the NC regime.[54]

Eventually, with grain size decreased significantly into the NC realm, grain size gets so small that deformation mechanisms other than dislocation movement can occur. Some alternate deformation mechanisms proposed for NC grains are diffusional creep, grain

boundary sliding, grain rotation, and twinning.[44] Some controversy has occurred as to whether these alternate deformation mechanisms actually cause strength to subside if grain sizes are on the small end of the NC range. The proposed drop in strength has often been termed an “inverse Hall-Petch” relation by those discussing it. Figure 10 is a result that illustrates a supposed inverse Hall-Petch behavior.

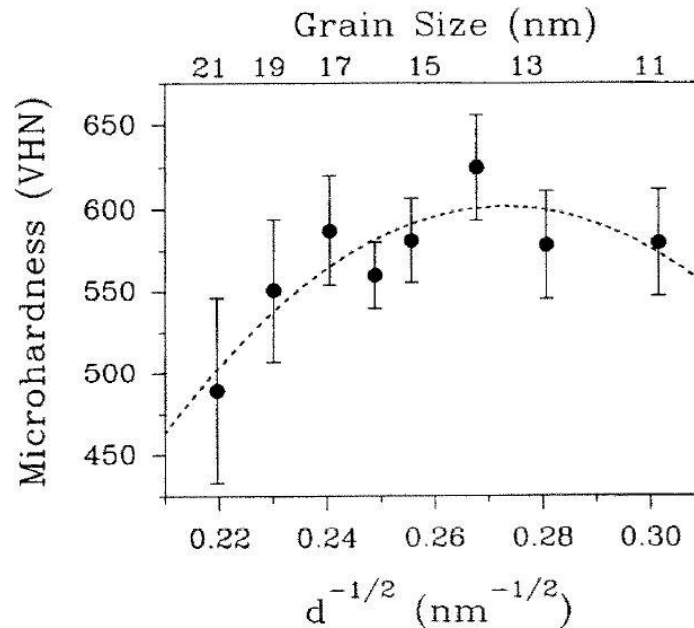


Figure 10. Hall-Petch effect for electrodeposited Ni-Fe. Transition from normal Hall-Petch material behavior to inverse Hall-Petch material behavior is claimed. [55]

In the case presented in Figure 10, the number of data points available to determine the dip in the end of the trend line doesn't seem conclusive. A trend line that levels off on a plateau seems equally credible. Meyers, et al. highlight several other studies from the literature which show even more dramatic strength declines on the small end of the NC grain size range.[44] However, many experts now have doubts about the appropriateness of the results and the existence of the inverse relationship. Porosity of samples, gaseous impurities, and

variation of composition within the samples are suspected as contributors to the early conclusions.[48]

2.5. Consideration of Amorphous Structure

Glazing is the melting of a substrate surface with subsequent ultra-rapid cooling to produce a non-equilibrium amorphous coating.[5] Amorphous materials are normally very resistant to deformation because dislocations cannot move through them. Creation of a metallic glass on the surface of a tool steel substrate may prove to be a very hard and wear resistant combination. However, ferrous materials, like most metals, are very resistant to amorphization because crystallization represents a lower energy state. An alloying of approximately 20 atomic % metalloids such as boron, phosphorous, carbon, and silicon is usually found to be necessary to allow amorphization of bulk ferrous alloys.[56] These metalloid elements are present at a much lower concentration in the S7 tool steel being studied, so glazing to create even a thin continuous amorphous surface would be difficult and unlikely. However, Zhang, et al., did report the presence of very localized amorphous regions as a result of e-beaming D2 steel. They believed extremely high carbon concentrations were achieved in locations where carbides were dissolved and instantly frozen before diffusion could occur.[23] Similarly, Tang, et al., found evidence of local amorphous regions along grain boundaries after e-beaming M50 steel.[19]

2.6. Residual Stress

The dynamic nature of the cooling gradients and phase changes in the beamed layer is capable of producing residual tensile stress.[3] Due to the very small melt thickness and the very short time durations, very large temperature gradients exist. In nearly all materials, a solid of unchanged phase expands with increasing temperature and contracts with decreasing temperature. A phase change occurring in the solid may also cause contraction or expansion depending on the packing factor of the involved lattice arrangements. Generally, adjacent layers that cool from significantly different temperatures will contract differently, which will produce detrimental residual tensile stress.[3][2] The residual stress from cooling gradients applies across a very large number of grains and can be termed a macrostress. The residual macrostress alters the general atom spacing in the crystal lattices. Conversely, microstress is localized around defects such as dislocations, vacancies, and other defects. Local instances of microstress will not affect the overall macrostress.[57] In this paper, any further mention and discussion of residual stress will refer to macrostress unless noted.

Figure 11 depicts a thin surface layer with residual stress. Commonly, surface residual stress is assumed to be planar and biaxial, acting across all grains with no component normal to the surface.[57] Contractions due to cooling are assumed to behave equivalently in the x and y directions. Thus, stresses in Figure 11 are defined as:

$$\sigma_z = 0,$$

$$\text{and } \sigma_x = \sigma_y.$$

Despite the assumed absence of direct strain normal to the surface, Poisson strain will still be developed in that direction. Poisson strain is the corresponding strain that occurs in the two principle directions normal to a direct strain. The Poisson strain will be of opposite sign to its corresponding direct strain and is quantified by the Poisson ratio, ν , for the material. The general equations for the total principal strains including the Poisson effect are shown next.[58]

$$\varepsilon_x = \frac{1}{E} [\sigma_x - \nu(\sigma_y + \sigma_z)]$$

$$\varepsilon_y = \frac{1}{E} [\sigma_y - \nu(\sigma_x + \sigma_z)]$$

$$\varepsilon_z = \frac{1}{E} [\sigma_z - \nu(\sigma_x + \sigma_y)]$$

The resulting strains and strain relationships for the condition in Figure 11 simplify as follows:

$$\varepsilon_x = \frac{1}{E} [\sigma_x - \nu(\sigma_y)],$$

$$\varepsilon_y = \frac{1}{E} [\sigma_y - \nu(\sigma_x)],$$

$$\varepsilon_z = -\frac{\nu}{E} (\sigma_x + \sigma_y),$$

where $\varepsilon_x = \varepsilon_y$.

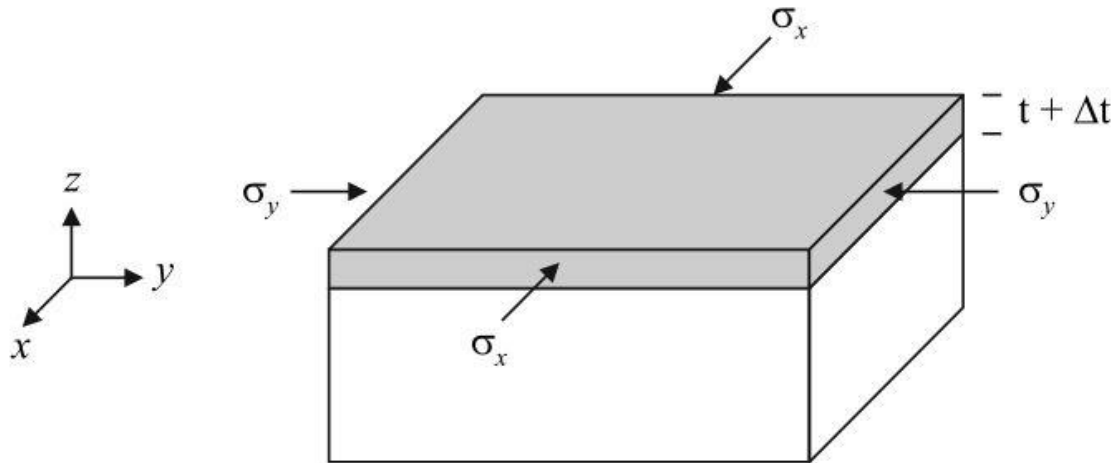


Figure 11. Depiction of plane stress in a surface layer
[59]

The Poisson strain in the z direction will modify both the layer thickness and the lattice spacing in the z direction. In Figure 11, the layer thickness change, Δt , is a result of the Poisson strain in the z direction with t representing the unstrained layer thickness. The orientation of each individual grain in the layer will determine the combination of direct strain and Poisson strain experienced by its lattice.[57] The effect of plane stress and Poisson strain on lattice spacing is illustrated in Figure 12. The 2-dimensional lattice illustrations represent grains in the surface layer which are oriented in various directions with respect to the surface. Without an acting stress, the lattice in each grain takes the normal lattice spacing, d_0 , for the material in its specific phase and at its specific temperature. All unstressed lattices in Figure 12 have the same lattice spacing, d_0 . If a stress is applied parallel to the surface, the lattice spacing in the direction normal to the surface is seen in Figure 12 to change to d'_0 due only to Poisson strain. The strain in the z direction is then:

$$\varepsilon_z = \frac{d'_o + d_o}{d_o}$$

The other depicted lattices in the stressed condition have orientations that allow them to participate to various degrees in both direct strain and Poisson strain due to the applied stress. The lattice spacing, d , will vary in each of these lattices, a condition which will be discussed in more detail in section 3.5.3.

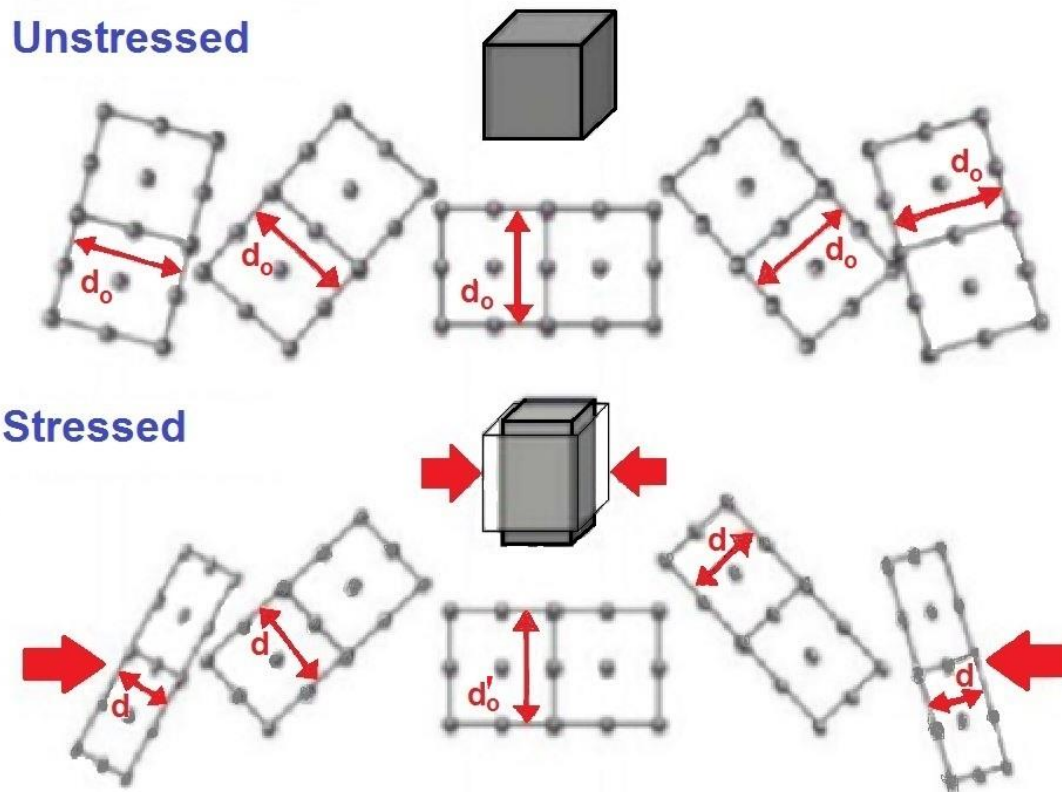


Figure 12. Schematic of stress effect on differently oriented lattices
- adapted from [60]

The creation of residual stress during e-beam processing has not been the topic of much study or experimentation. Proskurovsky, et al. was the earliest to assert that residual tensile stress was developed during the dynamic cooling of the e-beam melt.[2] Zhang, et al. used X-ray diffraction(XRD) to definitively determine residual stress developed during e-beaming of D2 tool steel under several processing conditions.[3] Figure 13 shows schematic representations of layer formation and stress distribution as determined by Zhang, et al. During melting, the liquid layer cannot maintain a stress. After cooling, Zhang's results show tensile stress extending all the way to the surface. Zhang also states that the stress distribution can be further complicated by the phase change and accompanying expansion from austenite to martensite during cooling.[3]

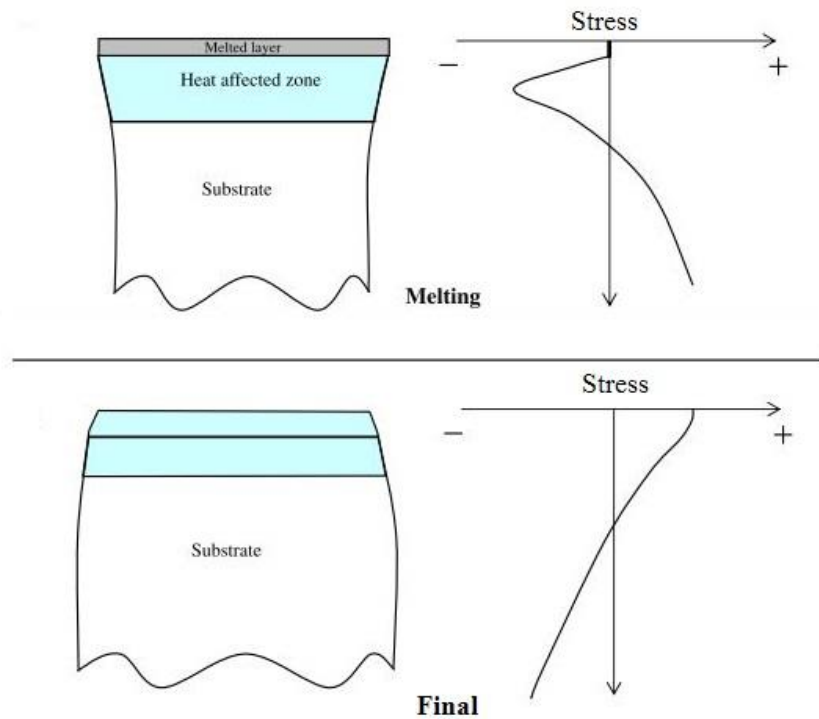


Figure 13. Schematic of expected stress states in e-beamed layers during melting and after conduction cooling to the substrate heat sink (surface cooling not considered)
[3]

As discussed in section 2.1, an alternate condition may be possible if surface cooling occurs rapidly enough to solidify the surface before the main melt layer. In this scenario, a very thin solid layer at the surface of the melt, like the original substrate, will reach a final compressive stress as the remaining melt layer cools. Deeper within the melted layer, the tensile stress will still form. The proposed stress profile developed by a solidification front starting on the surface is shown in Figure 14. Despite a compressive stress on the surface, high tensile stress still forms very near the surface.

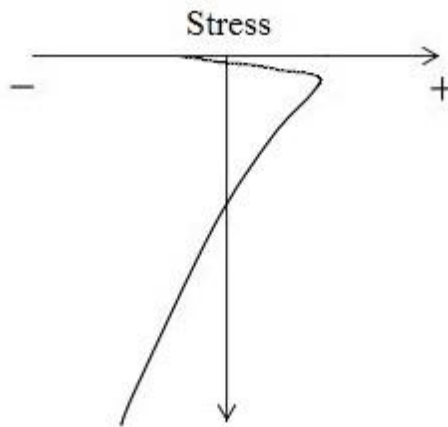


Figure 14. Stress pattern proposed for instance when solidification front starts on surface

Many studies have shown cryogenic freezing of bulk tool steels results in additional martensite formation.[61] The phase change from austenite to martensite includes an expansion which should counteract an existing tensile residual stress. An objective of this study is to utilize cryogenic temperatures to alleviate residual tensile stress reduction in e-beamed steel surface layers via expansion during phase transformation.

3. EXPERIMENTAL PROCEDURES

3.1. Tool Steel Specimens

Specimens were created from S7 tool steel, which is an iron alloy nominally containing (wt%) 0.5% C, 0.55% Mn, 0.6% Si, 3.25% Cr, 1.55% Mo, and 0.18% V.[62] The specimens were 6 mm thick and had a 16 mm x 16 mm surface ground to approximately 0.4 μm finish for e-beam treatment and study. A preliminary heat treatment was applied which consisted of austenitization at 940 °C, air quenching to room temperature, tempering at 315 °C, and then tempering again at 300 °C. Hardness readings between Rockwell C 54 and 56 after the heat treatment confirmed the process was correct. Figure 15 shows five specimens with the prepared surface facing up and one specimen flipped over to reveal the use of engraved identifying marks to help sample management.

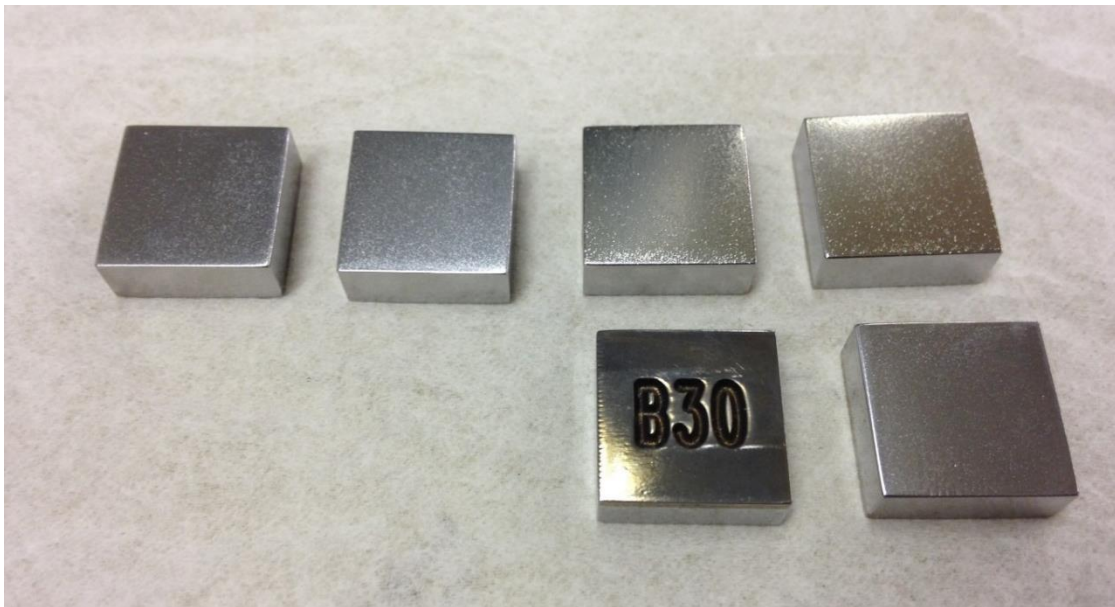


Figure 15. Specimens ready for e-beam treatment

3.2. Electropolishing

Electropolishing was used for cleaning, surface smoothing, and material removal during the experiments. Following the standard quench and double-temper heat treatment described in section 3.1, electropolishing was used to remove any surface oxides and provide further smoothing of the surface for improved testing. The potential for progressive smoothing of a surface during electropolishing is depicted in Figure 16. Several of the samples were reserved after this initial electropolishing step to act as controls for comparisons to specimens receiving the additional treatments. Electropolishing was also used during testing to remove precise, incremental amounts of material from the surface so that testing of properties at various depths could occur.

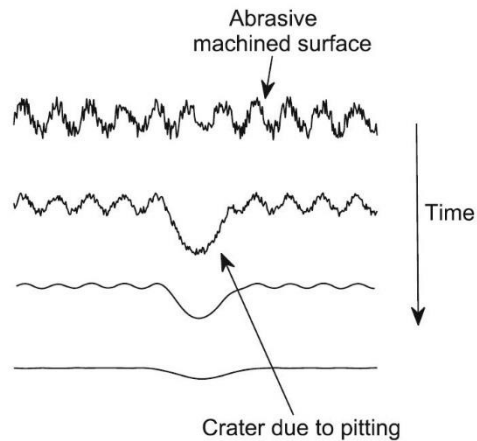


Figure 16. Schematic of surface finish improvement over time during electropolishing [63]

The electropolishing method needed to be optimized for the specific size and material of the specimens being treated. A schematic of the electropolishing process is shown in Figure

17. The developed method utilized a bath of commercially available electropolishing solution sold under the name EPS 4000, which consisted predominantly of phosphoric and sulfuric acids. The solution is available from Electro Polish Systems, Inc.; Germantown, WI, USA. As can be seen in Figure 18, electropolishing will only occur at specific voltage and current parameters. However, Figure 18 is general in nature; the electrical parameters need to be determined for each combination of alloy, bath chemistry, temperature, and geometry being considered. The process developed for the S7 samples used a 2.5 VDC potential and a polishing solution bath warmed to 80-90 °C. Following polishing, the specimens were rinsed as quickly as possible in deionized water followed by cleaning in a warmed, agitated detergent solution made with 398T from ACCU-LABS Inc., Chicago, IL, USA.

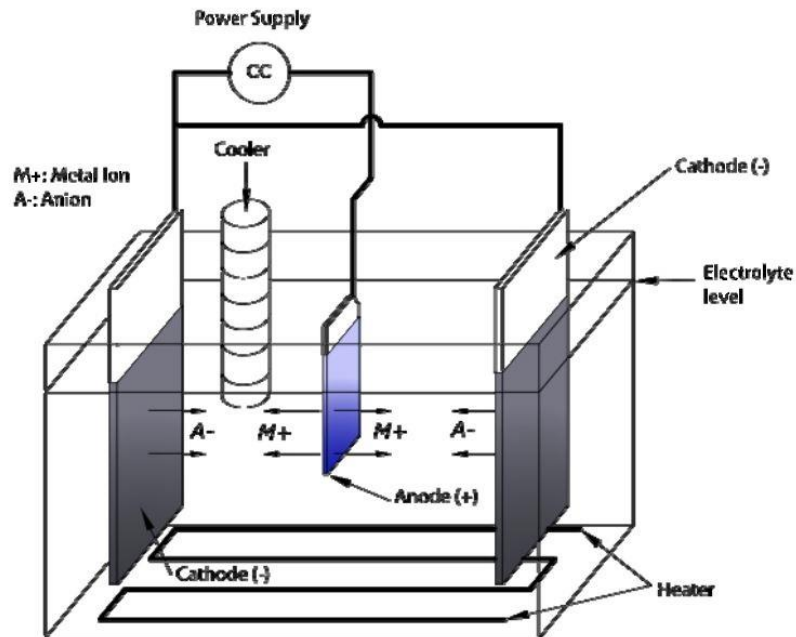


Figure 17. Schematic of typical electropolishing process [64]

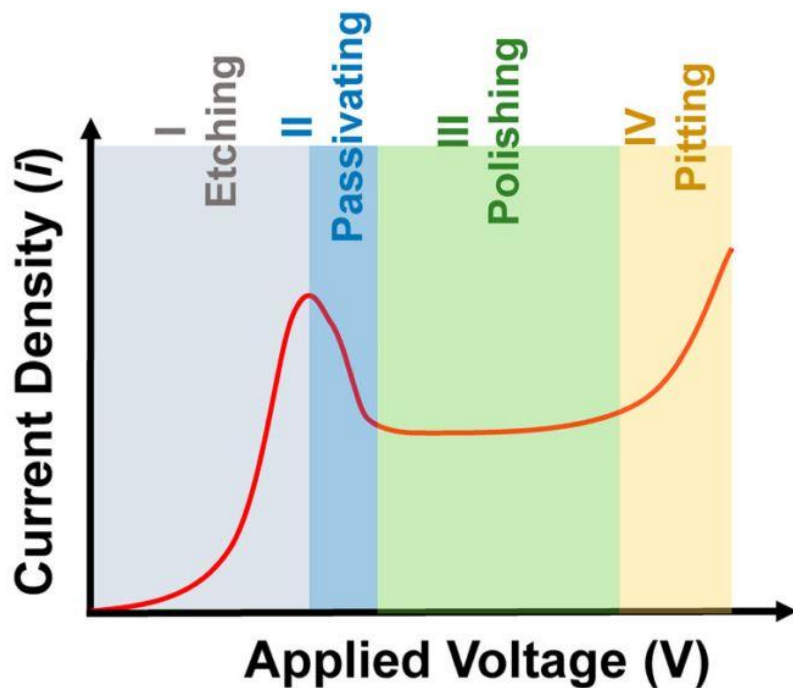


Figure 18. General current to voltage relationship for electrochemical treatments to metal surfaces [65]

To preserve a portion of a surface during the electropolishing process, masking was applied prior to immersion in the electropolishing bath. Common nail polish, based on nitrocellulose polymer, was found to be acceptable for masking if applied in several coats with each coat cured at 65°C for 20 minutes. Figure 19 illustrates the application of the mask and the result after 9 masking and polishing steps. Under each portion of the mask, the surface is preserved at the depth and condition existing when the mask was applied. If necessary or desired, the masking could be dissolved later with a solvent for additional tests or checks on the material at the depth represented by the preserved area.

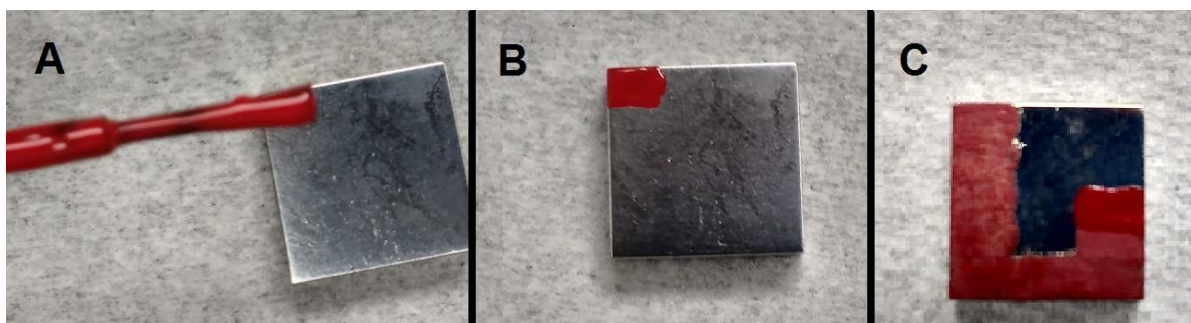


Figure 19. Masking of specimen during electropolishing
A) applying mask B) first mask applied C) multiple masks applied through multiple electropolishing steps

3.3. E-beaming Device and Process

A Sodick Co., Ltd., model PF-32B e-beam device, which can be seen in Figure 20, was used for the surface e-beam treatment. This model is of the wide-aperture, plasma-based type. The wide aperture allows up to a 60mm diameter area to be treated with a single pulse. Beam pulses are preset by the Sodick control software at 2 μ s duration. Argon at 0.05 Pa was used as the plasma gas. Initial experimentation determined that beam settings of 25 kV cathode voltage, 5 kV anode voltage, and a 30 mm gap between the anode and the specimen produced visual evidence of melting, shining, and smoothing on the surface. Therefore, these beam conditions were used for all the tests. Two sets of samples were created; one set received one e-beam exposure of the referenced e-beam pulse conditions and one set received 8 e-beam pulse exposures. When multiple e-beam exposures are used, the Sodick control software spaces the pulses several seconds apart so that substantially complete cooling occurs between each exposure.



Figure 20. The Sodick PF32B e-beam device used for surface treatment

3.4. Cryogenic Treatment

Some of the samples received a cryogenic treatment which began 4 days after e-beaming. The cryogenic freezing was carried out at $-196\text{ }^{\circ}\text{C}$ using liquid nitrogen in an insulated tank at atmospheric pressure. The samples were hung above the liquid in a basket fashioned from copper wire for several hours and then lowered into the liquid for approximately 2 days.

3.5. X-Ray Diffraction(XRD)

3.5.1. General Diffraction Principles

When a radiation wave encounters an electron that is tightly bound, much of the wave will be scattered elastically in all directions.[66] The scattering is accomplished because the changing electric field of the wave causes the encountered electron to instantaneously vibrate at an excited energy and then give off its own waves as it falls back to its normal energy.[58] Elastic scattering, also termed coherent scattering, implies that the new waves will be of the same phase and energy as the original beam. When waves from multiple collisions are scattered, there may exist some direction in which the waves have a constructive interference which is termed diffraction.[58][66] The illustration in Figure 21 will show the implications of scattering and diffraction on crystalline materials. When wave 1 in Figure 21 impacts atom K and wave 1a impacts atom P, waves will be scattered in all directions from each collision. Assuming wave 1 and 1' are in phase, there is only one direction where the scattered waves would remain in phase with each other. The paths labeled 1' and 1a' show the direction for which the path traveled by a portion of the scattered waves remains the same length. It can be proved mathematically that the length PR is the same as the length QK allowing the waves to stay in phase. The diffraction angle between 1 and 1' is twice as large as the incidence angle, θ , of wave 1 with respect to the surface. Because of the periodic spacing of atoms in a crystal, the portion of a wave scattered at an angle parallel to 1' from any atom on plane A will add to the diffraction intensity.

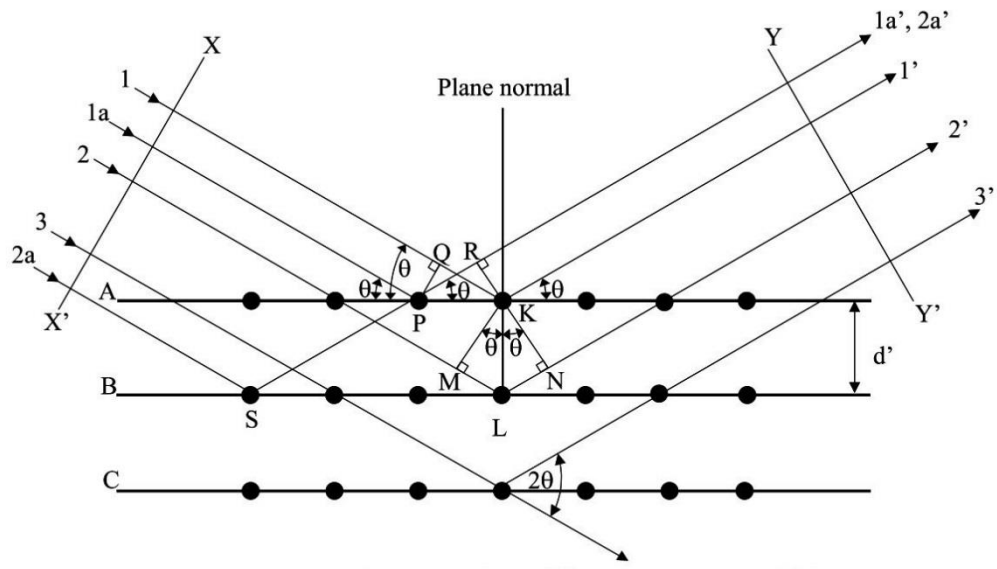


Figure 21. Diffraction of X-rays by a crystal lattice [67]

Under certain conditions waves from other planes of atoms can reinforce the diffraction. W.L. Bragg was the first to understand and quantify the conditions for diffraction reinforcement from other planes.[68] Bragg realized that if the difference in travel length of waves scattered from different planes was a whole integer multiplier of the radiation wavelength, then the waves would end up remaining in phase. His realization resulted in a formula, called Bragg's Law, which is at the center of X-ray diffraction theory and practice:

$$n\lambda = 2d\sin\theta.$$

The wavelength of the radiation is λ and n represents an integer. As was shown in Figure 21, d is the planer spacing in the crystal and θ is the incidence angle to plane A. Because lattice plane spacing distances commonly measure a few angstroms, the X-ray radiation band is found to have appropriate wavelengths to make use of Bragg's Law.[66] The planer spacing,

d, can be found with a known wavelength by incrementally searching through all possible angles to find angles for which Bragg's Law is satisfied and diffraction occurs.

A schematic of a basic XRD device is shown in Figure 22. Typically, the x-ray source, the detector, and the sample holder can all rotate to create different angles in the plane shown. Although not needed for the current work, many systems allow the sample to also be tilted in other directions out of the plane shown. Diffraction will be noted by peaks in intensity registered by the detector at the angles at which Bragg's law is satisfied. Common crystal lattice systems will have multiple plane directions displaying periodicity, so multiple sets of diffraction peaks are likely to be found. Figure 23 shows an example XRD output for a single-phase substance showing diffraction peaks for planes with various Miller indices. Using Bragg's law, the plane spacing, d, for the various plane systems can be found. Similarly, if the plane spacing is known, the diffraction peak angles, θ , can be predicted from Bragg's law. In polycrystalline material, only those grains whose planes are properly aligned will participate in diffraction.[69] If the grains are randomly oriented, the results from the diffracting grains accurately represent the entire population of grains within the material.

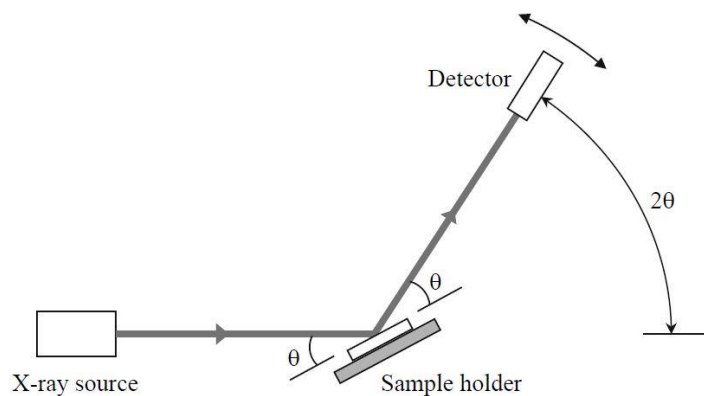


Figure 22. Schematic of basic X-ray diffraction device [59]

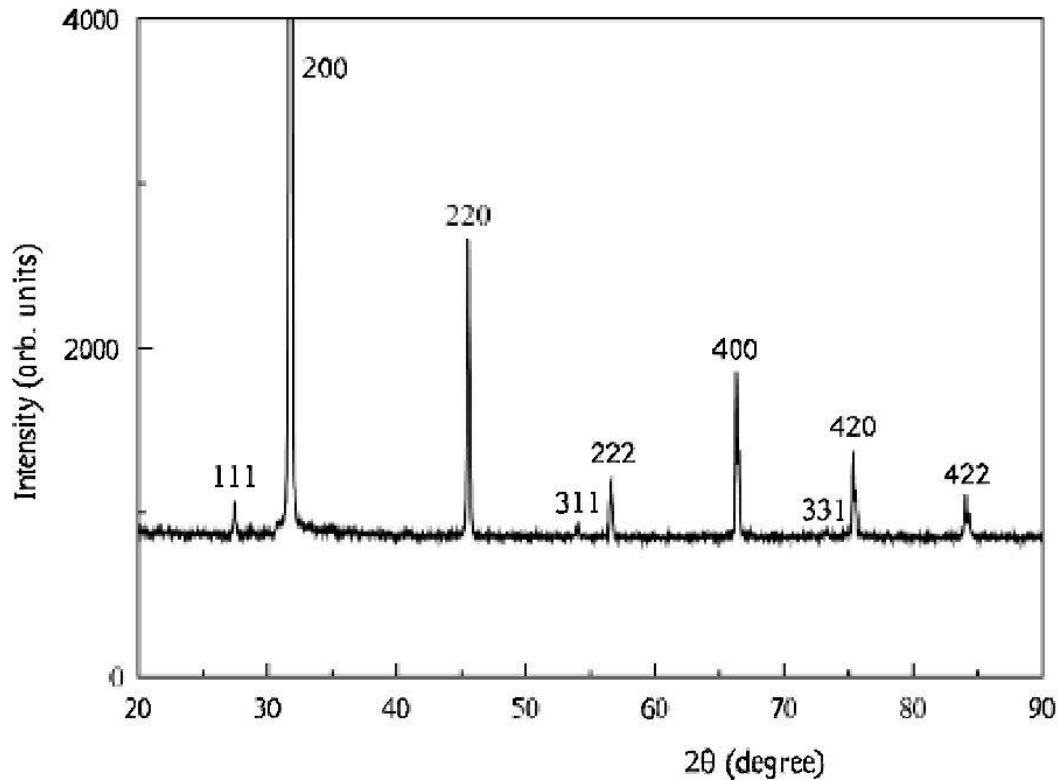


Figure 23. X-ray diffraction scan of a single-phase solid(NaCl) illustrating intensity peaks for different plane systems [59]

3.5.2. X-Ray Diffraction for Phase Identification

The principles discussed in section 3.5.1 and highlighted with Figure 23 also apply to solids with multiple phases. Each phase will produce its own set of XRD peaks when the sample is analyzed. For example, Figure 24 from Talebi, et al. shows that tempering of a medium-carbon, low-alloy steel resulted in the precipitation of carbide phases which produced their own XRD peaks. The new peaks arise because the lattice arrangement in the new phases is different than the lattice arrangement in the original phase. As discussed in section 2.3, heat treatment of steel may produce several phases including carbides.

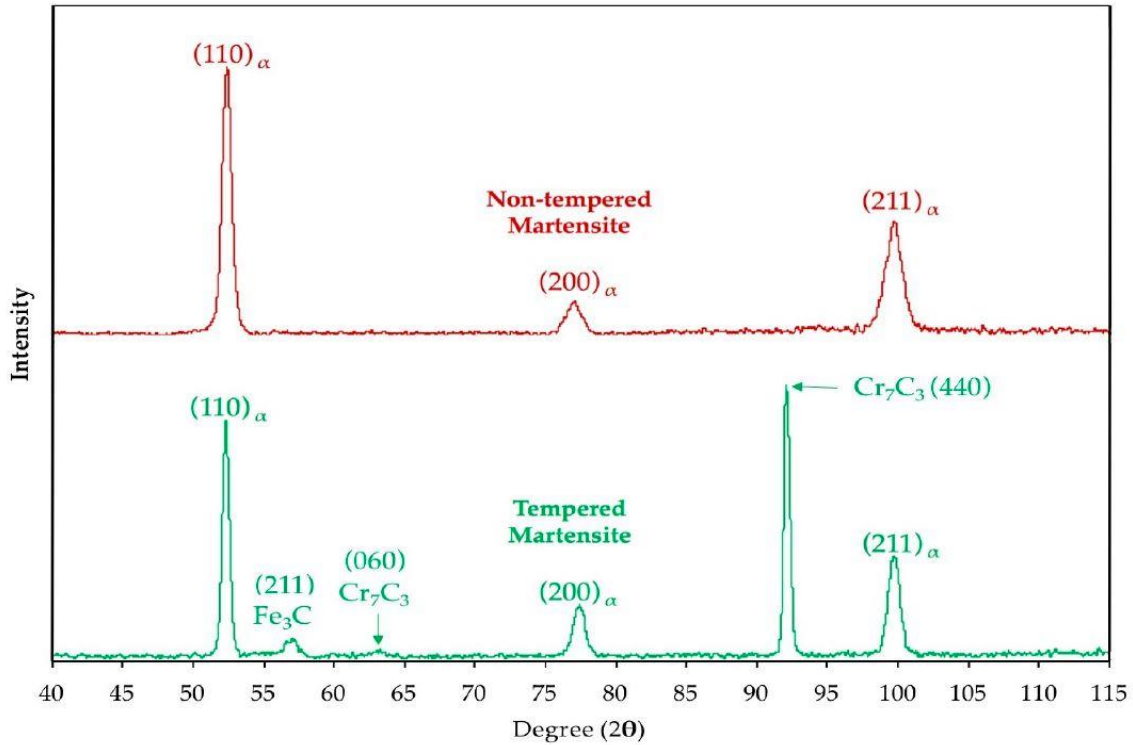


Figure 24. XRD results of medium carbon, low alloy steel at 2 stages of heat treatment [70]

A sample treated with a single e-beam pulse and an unbeamed control sample were both analyzed for retained austenite content using an XRD technique. The XRD analysis was carried out by an accredited laboratory following an established ASTM standard, E975. [71] Figure 25 shows one of the samples mounted for XRD determination of retained austenite. The ASTM E975 method utilizes the intensities from 4 total diffraction peaks of chromium $K\alpha$ irradiation. Specifically, the peaks studied are at $2\theta = 78.5^\circ$ for austenite (200), $2\theta = 106^\circ$ for ferrite/martensite (200), $2\theta = 128^\circ$ for austenite (220), and $2\theta = 156^\circ$ for ferrite/martensite (211). Additionally, corrections are made to account for certain carbides which, if present, may add to the apparent intensity of some of the peaks being evaluated. The correction is

usually made by software that can detect and evaluate separate peaks that quantify the presence of common error-inducing carbides. Carbides known to affect the 4 studied peaks include Fe_3C , M_6C , Cr_3C_2 , Cr_7C_3 , and M_{23}C_6 . [71] Chromium radiation is appropriate for samples containing iron to avoid high fluorescence that can occur with the more common copper radiation. [57] The austenite content of the e-beamed sample was determined at progressive depths by electropolishing to remove material between subsequent XRD tests. Electropolishing allows the removal of material in the most stress-free means possible so that the newly exposed layer remains essentially unaltered from its original state. Stress from other removal methods may initiate a phase change and thus skew the results. [71]

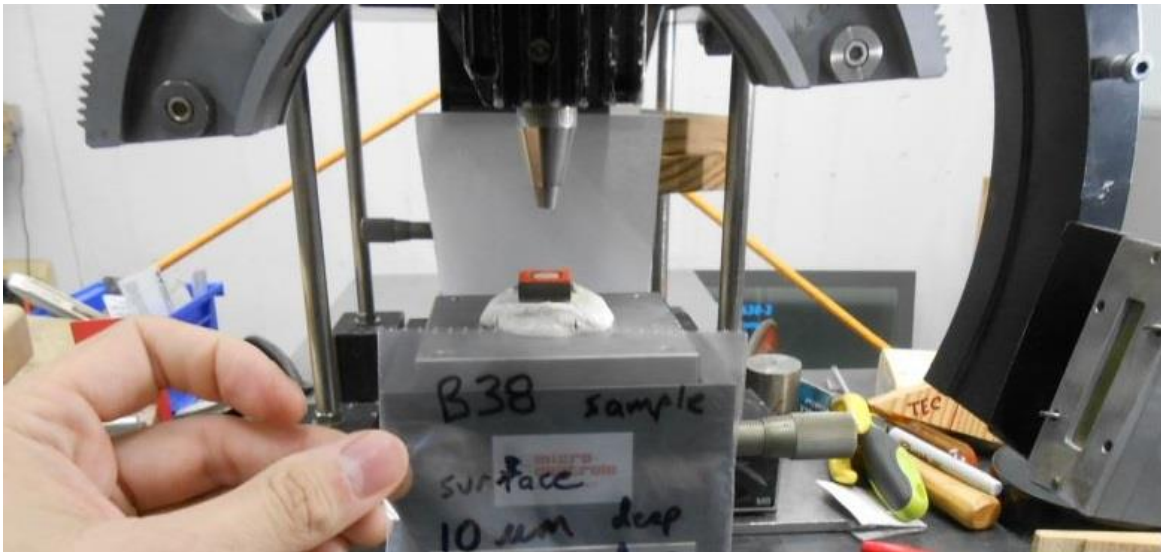


Figure 25. Sample mounted in the XRD equipment for retained austenite determination

3.5.3. X-Ray Diffraction for Residual Stress Determination

The use of XRD to evaluate residual stress hinges on detecting the change to the lattice spacing under the applied stress. Section 2.6 discussed background information on stress-induced lattice spacing changes. From Bragg's Law, presented in section 3.5.1, a change in lattice spacing, d , necessitates a change in diffraction angle, θ . Figure 26(a) and (b) illustrate the change in diffraction angle under a residual macrostress. As an aside, Figure 26(c) illustrates the XRD peak change that occurs due to microstress.

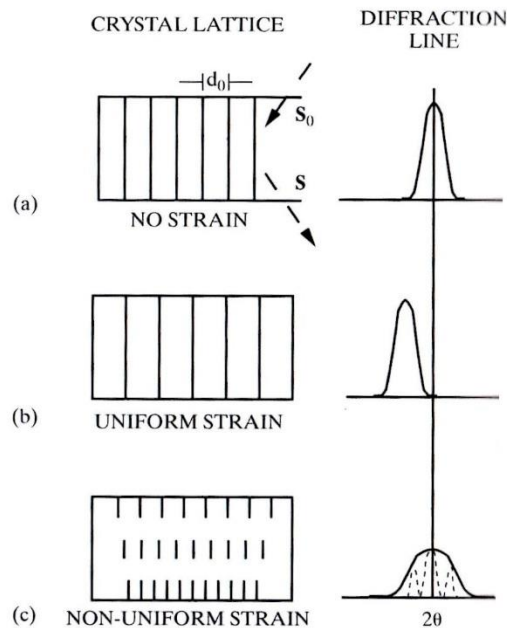


Figure 26. Changes to XRD diffraction peak under strain
[67]

The measurement of lattice spacing is not straightforward because the orientation of the grain will affect how the lattice participates in direct and Poisson strain due to a planer

residual stress. To evaluate the stress on an overall basis involves the use of a tilt angle being utilized in the XRD equipment. Referring to Figure 27, the angle Ψ will be defined as the tilt angle between the normal to the surface and the normal to the diffraction plane. The normal to the diffraction plane also is the axis of symmetry between the incident beam and the diffracted beam. The illustration shows the beam and detector being tilted, however, the specimen could be tilted instead. For every angle Ψ , there will be a few grains in the specimen surface layer whose lattices are oriented for diffraction. Each grain oriented to a specified diffraction tilt will have a unique lattice spacing, d_{Ψ} , based on the magnitude of direct and Poisson strains it is experiencing. It can be shown[68] that a relationship exists between stress, σ , tilt angle, Ψ , and lattice spacing, d_{Ψ} , such that

$$\sigma = \frac{E}{(1 + \nu)\sin^2\Psi} \left(\frac{d_{\Psi} + d'_o}{d'_o} \right).$$

A further simplification is used in practice where the slope, m , of the d_{Ψ} versus $\sin^2\Psi$ is substituted without introducing more than .1% error[67][72]:

$$\sigma = \frac{E}{(1 + \nu)} m .$$

The plot of d_{Ψ} versus $\sin^2\Psi$ is found to be linear for biaxial stress and common materials free of significant texturing.[67] An example linear plot for d_{Ψ} versus $\sin^2\Psi$ is included as Figure 28.

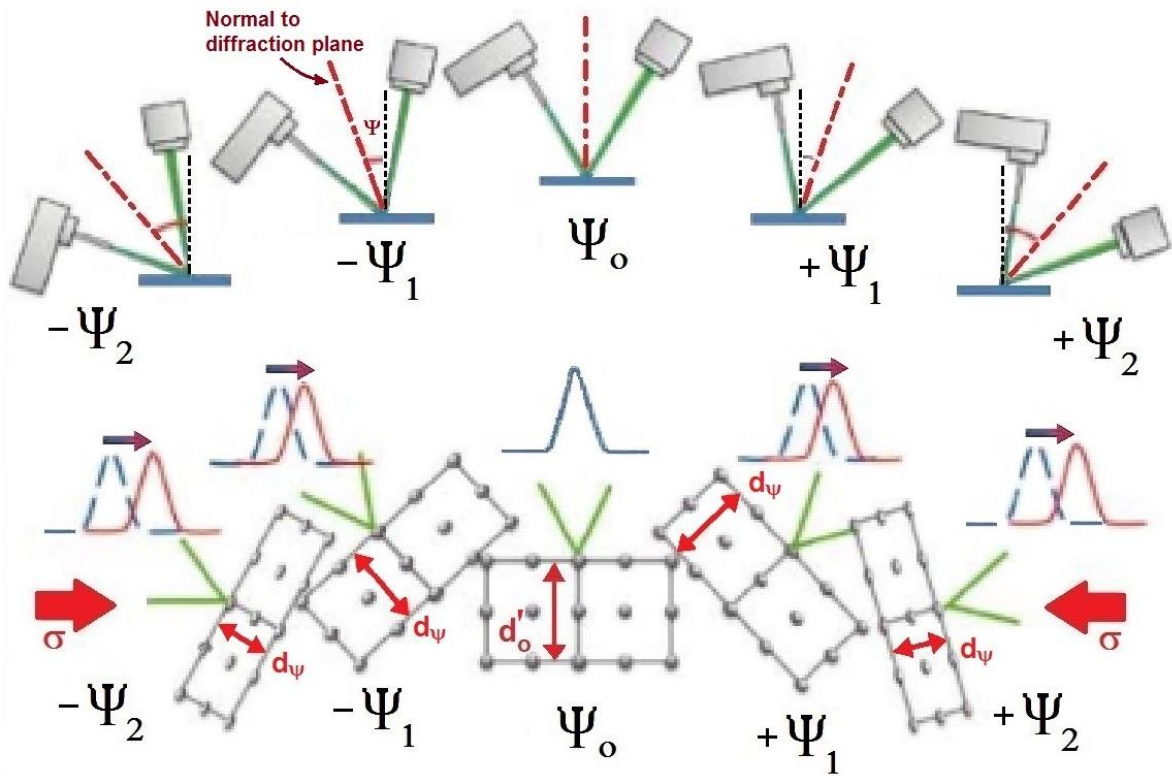


Figure 27. Schematic illustration of XRD Ψ rotations and diffraction peak movement under stress - adapted from [60]

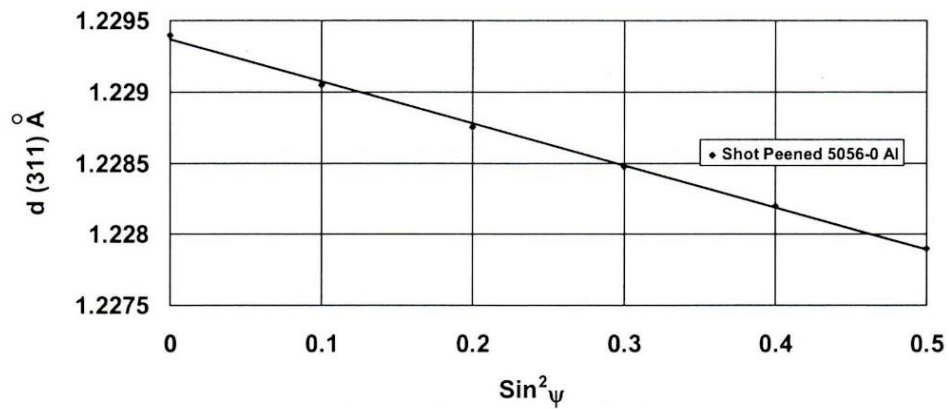


Figure 28. Example of linear d vs. $\sin^2\Psi$ plot used to determine m [57]

A second set of the e-beamed samples were subjected to an XRD $\sin^2 \Psi$ analysis of the residual stress according to the guidance of SAE specifications J784a and HS-784.[73][74] The samples included an unbeamed control specimen, a specimen treated with one e-beam pulse, a specimen treated with 8 e-beam pulses, and a specimen treated with 1 e-beam pulse as well as subsequent cryogenic freezing. Chromium $K\alpha$ irradiation was used to study the spacing of the (211) plane of ferrite/martensite. Due to expected linearity of the $\sin^2 \Psi$ versus strain plot for common tool steels under planer stress, the two-angle simplification of the technique was appropriate. Specifically, Ψ angles of 10° and 50° were used. As explained by Prevey, stress gradients and x-ray penetration vary with depth necessitating a correction integration.[57] The integration is performed with processing software in the XRD equipment. An additional correction is also employed due to stress relaxation as a result of material removal, however this correction is negligible when the thickness removed is several orders of magnitude less than the thickness of the total sample.[57] The XRD residual stress determination was carried out by a second accredited laboratory.

3.6. Nanoindentation

The common hardness testing methods and devices can be grouped by the magnitude of the load and size of the indent. Table 2 lists general groupings of common indenting methods and scales from the coarsest to the most delicate. The standard and superficial test scales are rather prolific in everyday industry but are not adequate for fine work on very thin layers such as are found in this investigation. The Knoop and Vickers microhardness tests are much more delicate but require manual optical measurement. For very fine features and

very thin layers, nanoindentation methods have been developed which are superior to even the microhardness tests. The advantages of nanoindentation include smaller loads, shallower indentations, direct measurement, and continuous monitoring of load and position during the entire indentation procedure.[75]

Table 2. General classification of hardness testing methods

Hardness Test Class	Example scales	Comments
Standard	Brinell[76] Rockwell B, C[77]	Inexpensive, easy to operate, wide industrial use, load > 60 kg
Superficial	Rockwell N and T series[77]	Inexpensive, easy to operate wide industrial use, load = 15 – 45 kg
Microhardness	Knoop[78] Vickers[78]	Optical measurement required, load <= 1000g
Nanoindentation	specialized	Expensive, specialized equipment, load generally measured in mN

Optical measurements are time-consuming and can lead to error and resolution problems. Depending on the work-hardenability of the material, indentations may form pile-up or sink-in around the indenter as illustrated in Figure 29. Determination of the bounds of the included area in optical area measurement may not be straightforward in these cases. As indents get very fine, errors due to this uncertainty can be large. Also, finding very small indentations in the optical view after they are created may be difficult.[75] Nanoindentation methods overcome the problem of reliance on optical measurement that can exist in the Knoop and Vickers microhardness methods.

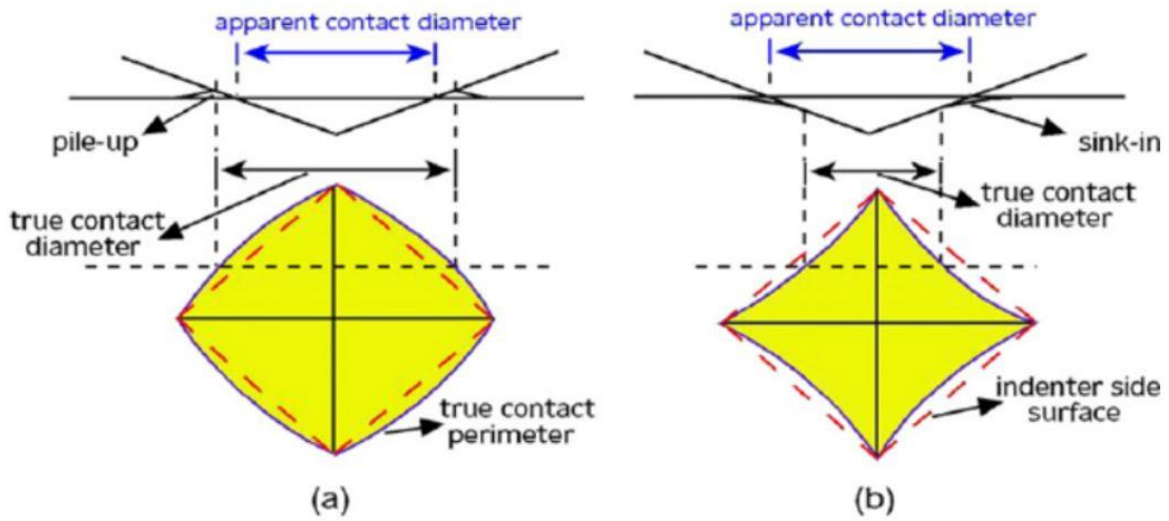


Figure 29. Illustration of pile-up and sink-in phenomena as a result of indentation [79]

Figure 30 shows a representative load and unload curve illustrating the continuous data collection during typical nanoindentation measurements. In addition to hardness, the theoretical elastic modulus can be calculated from the initial slope, S , of the unload portion of the curve shown in Figure 30.[80] The loading and unloading should be done very slowly in order to improve the certainty about when contact was established and to avoid heat buildup in the local contact area.[81]

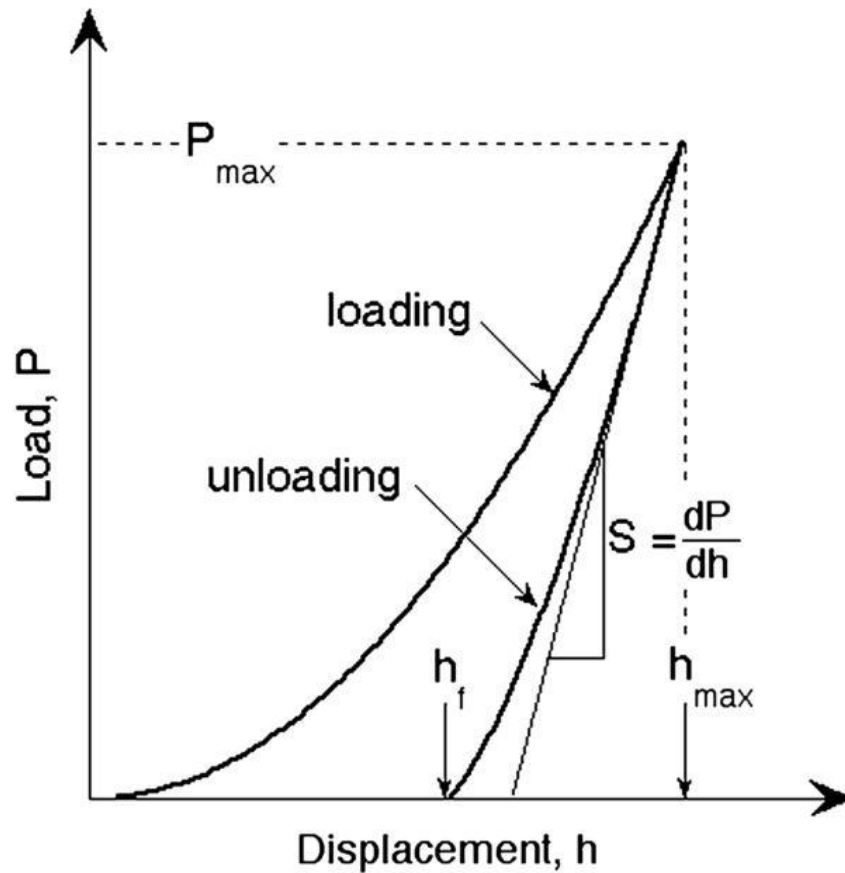


Figure 30. Schematic of load and unload data curve for nanoindentation [80]

A common indenter used for nanoindentation was proposed by E. S. Berkovich [82] and is named after him. Figure 31 shows atomic force microscopy (AFM) images of an actual Berkovich indenter at 2 different magnifications. The original Berkovich indenter was 3-sided with a face angle of 65.03° which was a design created to have the same ratio of indentation depth to actual face contact as the Vickers indenter.[82] Berkovich realized that a 4-sided indenter such as a Vickers indenter is difficult to form to a perfect point. As shown in Figure 32, manufacturing error is likely to create an offset of some size on a 4-sided

pyramid. When working with very small indentations, this offset may be a large percentage of the indentation size. A three-plane pyramid will always form a theoretical sharp point. The Berkovich indenter used most often today has been modified very slightly to a 65.3° face angle so that its depth to projected area ratio theoretically matches the Vickers indenter.[83] Both 3-sided and 4-sided pyramids face the problem of imperfect sharpness with a radius forming on the tip at some scale. The tip radius, which can be seen on the tip in the very high magnification of Figure 31b, can be due to wear or manufacturing imperfection. A calibration procedure is utilized to account for the actual contact area versus indentation depth of slightly rounded indenters. Calibration procedures are performed regularly to keep up with the condition of the indenter.

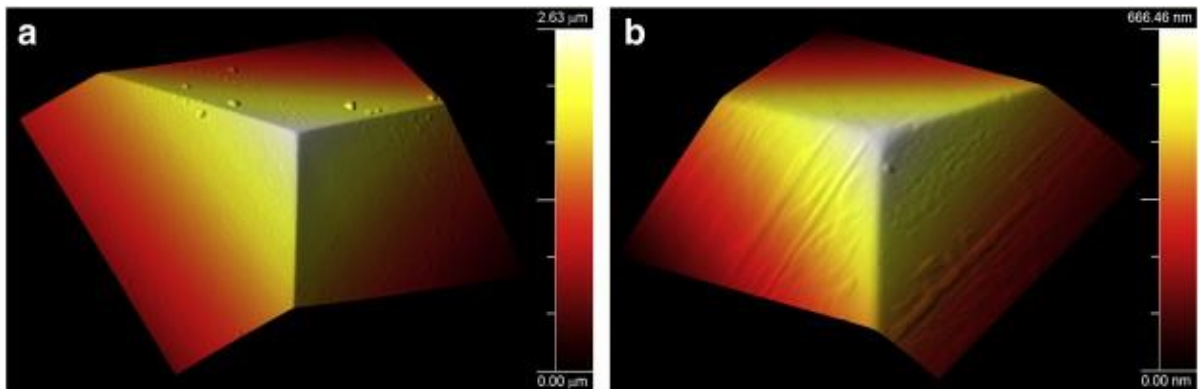


Figure 31. AFM images of a Berkovich-type tip
a) $10\ \mu\text{m} \times 10\ \mu\text{m}$ AFM scan. B) $2.5\ \mu\text{m} \times 2.5\ \mu\text{m}$ AFM scan.[84]

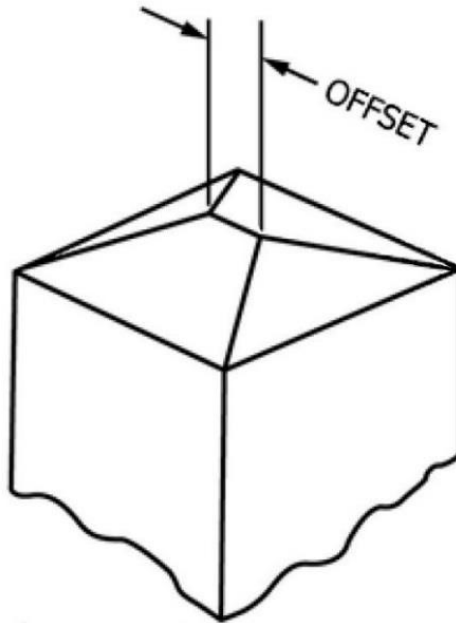


Figure 32. Illustration of malformed 4-face indenter [78]

To determine a hardness profile through the e-beamed layer, a procedure of alternating nanoindentation and electropolishing was devised. Samples treated with one e-beam pulse and 8 e-beam pulses were tested by this method. Also, a sample treated with each pulse count was tested in combination with an additional cryogenic freezing treatment. A Universal Material Tester(UMT) manufactured by CETR of Campbell, CA, USA was configured to do the nanoindentation testing. (Since 2011, CETR is owned by Bruker Corporation.) Indentations were made with a Berkovich indenter pushed with a 50 mN load. The 50 mN load created indents less than 1 μm deep in the specimens being studied. At various depths within the layer, 7 to 9 nanoindentations results were averaged to determine the reported nanohardness. A typical set of load curves for the procedure are depicted in

Figure 33. Several representative indentations were imaged by atomic force microscopy (AFM) and are shown in Figure 34. After gathering each nanoindentation data set, a portion of the surface was masked for preservation, and the remaining surface area was electropolished to a new depth.

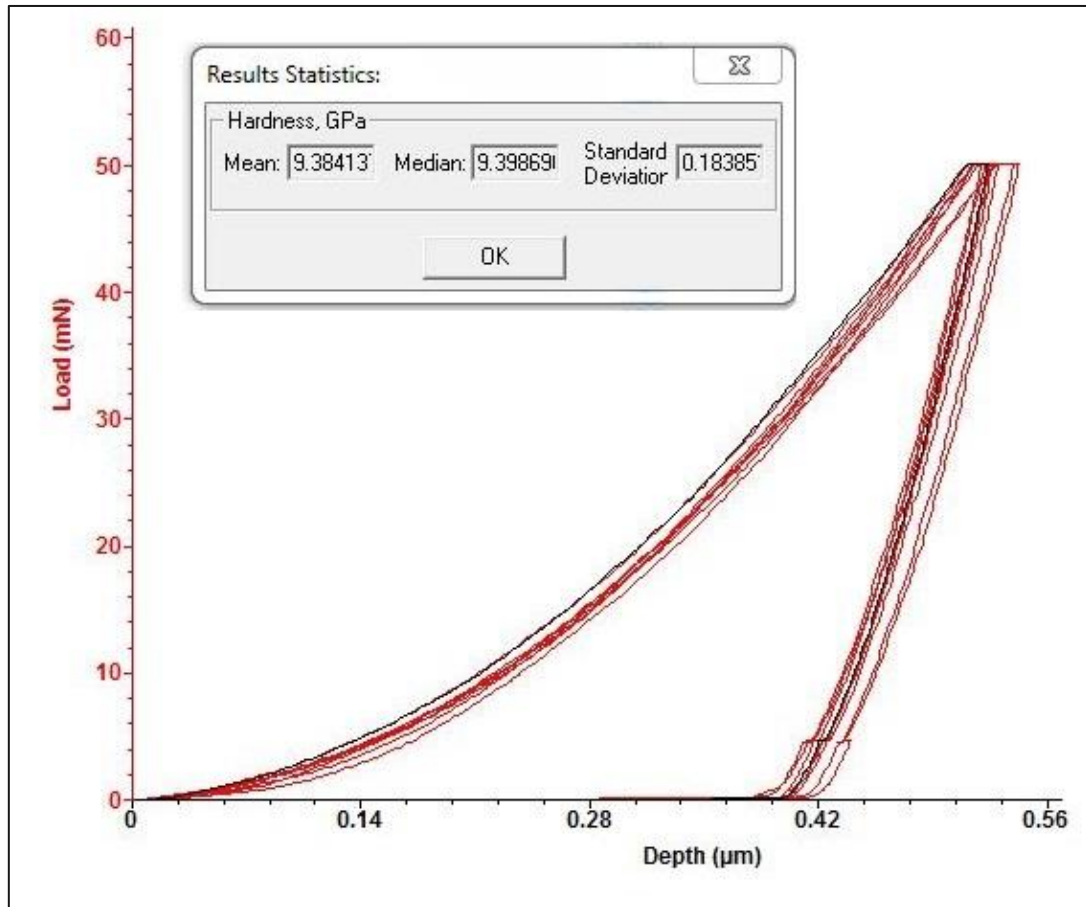


Figure 33. Representative load curves for a set of 50mN indentations with Berkovich indenter

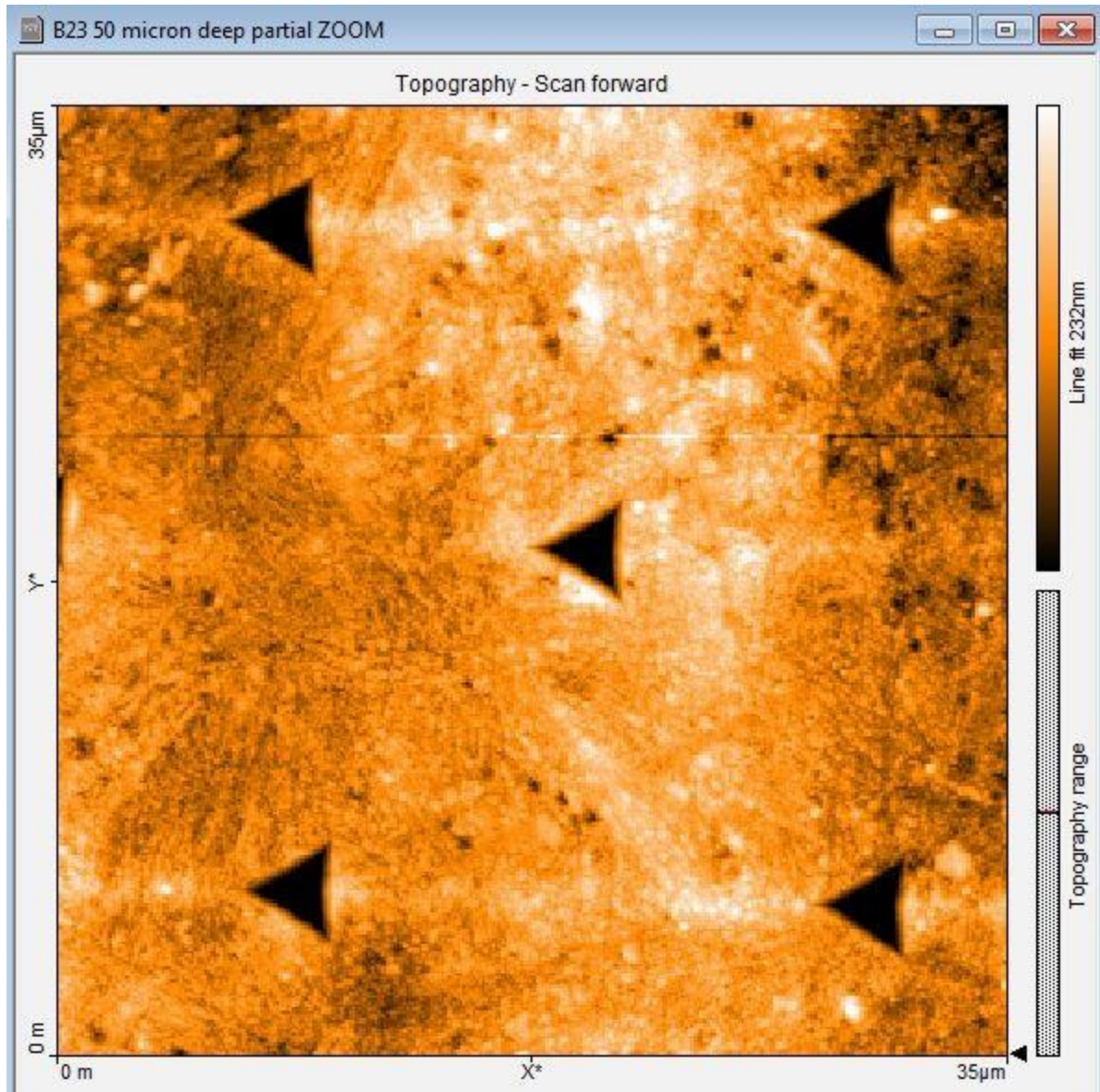


Figure 34. AFM scan of several representative nanoindentations in a specimen

3.7. Grain Size

The electropolishing process often produced enough of an etching effect to reveal grain morphology. The etching started at the end of the process as voltage fell off from polishing voltage and continues during the brief time it took to get the sample rinsed with deionized

water. To estimate the grain size, the etched surface was viewed via an AFM scan after a depth of 2 μm had been electropolished from the original surface. The AFM module was manufactured by Nanosurf, AG, of Leistal, Switzerland. The device was operated in tapping mode and a view area of 5 μm by 5 μm was used for grain size determination.

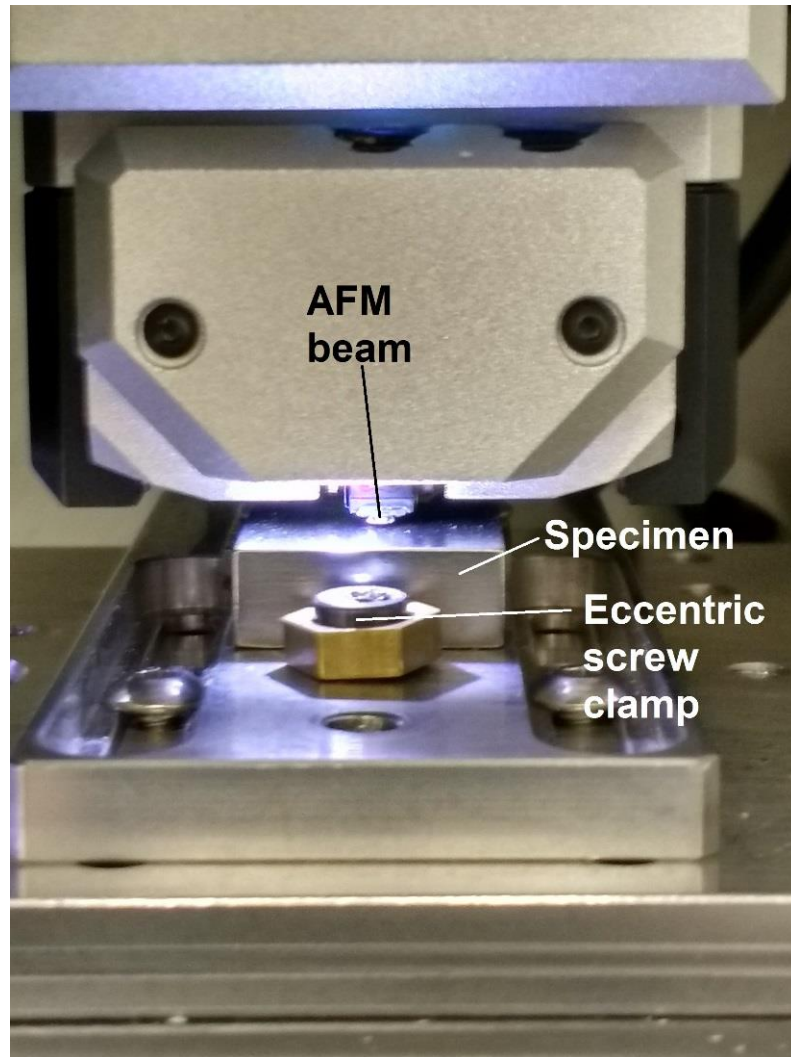


Figure 35. Specimen clamped in AFM unit for scanning of grain size and nanoindentation size

3.8. Coefficient of Friction

The coefficient of friction testing also made use of the UMT equipment from CETR/Bruker. The test equipment was reconfigured as depicted in Figure 36. As in nanoindentation, the z carriage provided ultra-precise z-direction movement with z-position feedback. The z-carriage was fitted with a load sensor capable of measurement of load in both the x and z directions. Below the load sensor, a mechanism is used to clamp a tungsten carbide (WC) ball which will serve as the contact point for sliding. The WC ball is clamped to prevent rolling. A module with a linearly reciprocating mechanism was installed under the carriage capable of precise z direction movement. The mechanism is a motor driven slider-crank mechanism producing approximately simple harmonic motion over 10mm of stroke in the x direction.

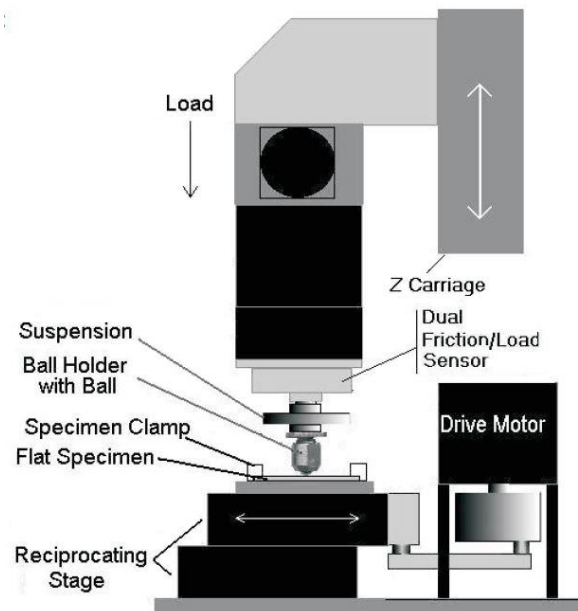


Figure 36. Schematic of tribological testing equipment for determination of coefficient of friction [85]

Figure 37 shows a sample installed for the friction test. The specimen is clamped from the side surfaces to a tooling plate on top of the reciprocating mechanism. The WC ball will remain stationary in the x direction but will move as necessary in the z direction to engage the sample and maintain the desired load. A 2N load and a 2Hz driving frequency were chosen for this test. The test continues through a 2 second acceleration, a 20 second dwell at speed, and a 2 second deceleration.

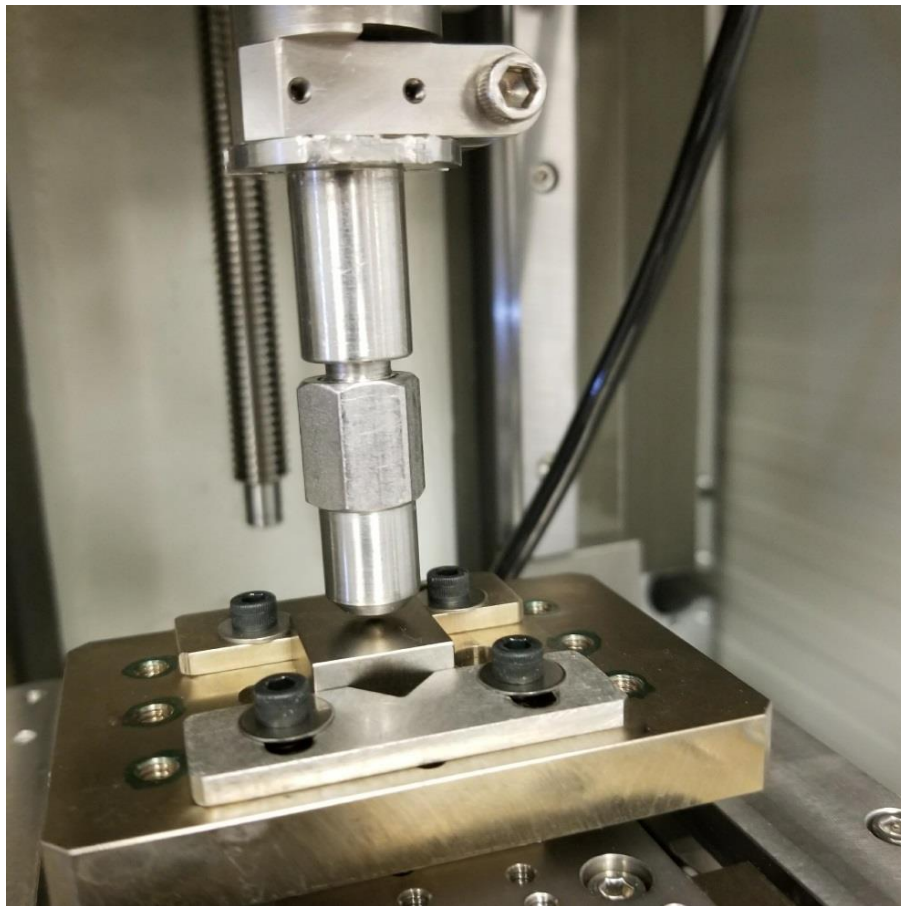


Figure 37. View of tungsten carbide ball in holder and engaging test sample during friction coefficient test

4. RESULTS AND DISCUSSION

4.1. XRD Analysis for Retained Austenite

The rapid melting and cooling of the e-beam treatments can be used to tailor the resulting microstructure via the introduction of crystal defects and non-equilibrium structures. When very rapid quenching of austenite occurs, it usually transforms substantially into metastable martensite; however, some austenite may be retained. Although both martensite and retained austenite are non-equilibrium microstructures, retained austenite has higher internal energy and is farther from equilibrium.

Figure 38 documents the XRD phase analysis carried out per ASTM E975 methods. Significant elevation of the austenite content is seen to a depth of at least 20 μm . The retained austenite content at a depth of 50 μm appears to have been unaltered and is of the same magnitude as the original retained austenite content of the unbeamed control. Other studies done on tool steel have shown similar findings of elevated austenite in the e-beamed layer.[3][26][29][31][33] Consequently, austenite for the proposed tensile stress reduction technique is likely to exist in the melt layer of e-beam treated tool steels. Generally, the lower the quenching temperature, the more complete the martensite conversion. Coaxing this retained austenite to transform into martensite with a cryogenic treatment should be a viable method for reducing residual tensile stress.

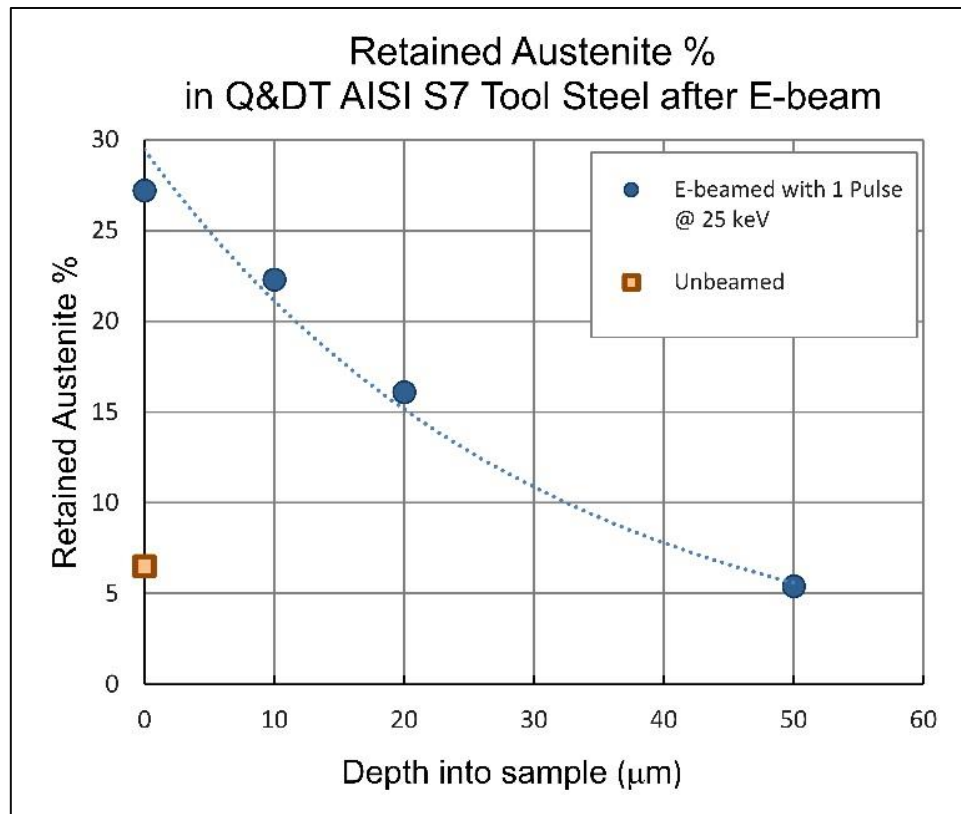


Figure 38. Retained austenite at various depths in e-beamed layer

The existence of increased retained austenite as shown in Figure 38 likely derives from the high carbide content in the original tool steel. Experiments have shown that with repeated e-beam pulses, the carbides can be completely dissolved into the melted layer.[20][3] With each melt sequence it is estimated that any released alloying elements from the carbides can diffuse on the order of 100 nm.[33] With a large number of repeated melt sequences, a homogenous layer containing the elements from the fully dissolved carbides will be formed. The homogeneous layer will have a different composition than the steel substrate which surrounds the carbides in the unmelted substrate.[19] Elevated alloying content can lower the finishing temperature of the austenite to martensite reaction to below

room temperature. For instance, Zou et al. proposed that dispersed alloy elements from the melted carbides contributed to stabilization of austenite in e-beam treated D2 tool steel.[28] Thus, multiple beam exposures are likely to produce more available retained austenite for the proposed stress reduction mechanism.

4.2. XRD Analysis for Residual Stress

The two-angle $\sin^2 \psi$ XRD results for residual stress versus depth into the sample is plotted in Figure 39. The e-beamed samples showed a very thin compressive residual surface stress. However, a high tensile stress peak over 1000 MPa was found at a depth of just a few μm below the surface. As was shown in Figure 38, considerable retained austenite is present at the same depth as the high tensile residual stress. Consequently, cryogenic freezing was employed to try to coax further conversion of austenite to martensite with the expectation that the martensite expansion would reduce tensile residual stress. A sample which had received one e-beam pulse at the referenced conditions followed by liquid nitrogen treatment was analyzed for residual stress using the same lab and procedures. A 28% reduction in peak tensile residual stress was revealed as shown in Figure 39.

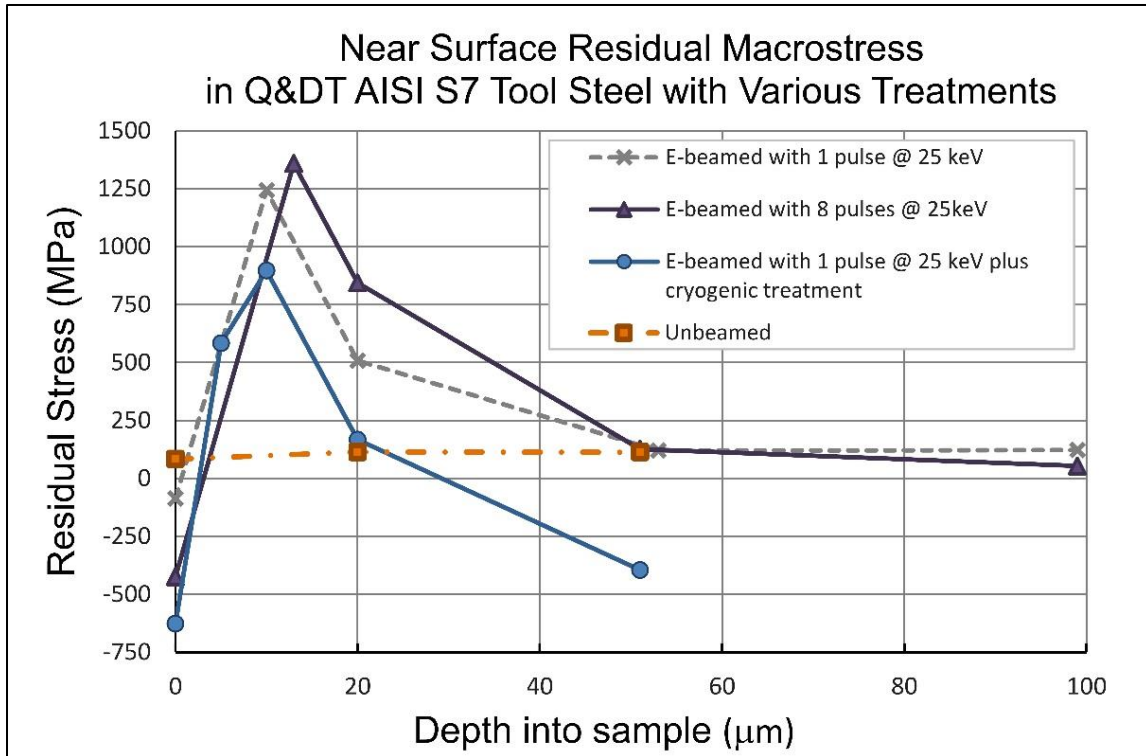


Figure 39. Residual stress in e-beamed samples as determined with XRD analysis

The compressive surface stress highlighted in Figure 39 would seem to indicate a solidification front started at the surface and moved into the melt slightly before the solidification front from the unmelted substrate arrived at the surface. As material under the surface contracted with cooling and solidification, the already solid surface was placed in compression. Surface compressive stress is usually an advantage and is not universally seen in e-beamed tool steel; for instance, Zhang, et al., found tensile stress on the surface for their treatment of D2 tool steel.[3] Despite the worthwhile presence of compressive surface stress, very high tensile stress just below the surface could still be problematic in some applications. The results in Figure 39 show that the hypothesis of reducing residual tensile stress with

cryogenic freezing was achieved. The proposed mechanism for the reduction was the coxing of the higher than usual quantities of retained austenite to expand due to a phase change to martensite driven by low temperature treatment. The low temperature treatment in combination with e-beaming for the purpose of stress reduction appears to break new ground. Zou, et al. did use cryogenic freezing on e-beamed D2 tool steel samples for a different purpose.[28] They were attempting to prove that they had stabilized austenite to the point that it wouldn't transform to martensite at 77K; no stress studies were done.

4.3. Nanohardness

All the e-beam treated samples show a significant hardness increase on the surface and to a depth of 3 to 5 μm . Table 3 records the surface hardness gains for each of the treatments. All the treatments showed hardness gains which ranged from 9.9 to 36.1%. The sample that received multiple e-beam pulses with subsequent cryogenic treatment shows the greatest hardness increase. The general trends are that an increased number of beam exposures creates higher hardness as does the addition of cryogenic treatment. The detailed results for nanohardness versus depth for each sample are shown in Figure 40 through Figure 43. The two samples that received 8 e-beam pulses seem to show deeper hardening profiles. The elevated hardness for samples receiving one pulse extended to a depth of 2 μm whereas elevated hardness extended to 5 μm for the samples receiving 8 e-beam pulses. The material hardness seems to be relatively unaffected by the treatments from a depth of about 25 μm and beyond.

Table 3. Surface nanohardness with various treatments

Sample	Average Surface Nanohardness (GPa)	Surface hardness increase (%)	Comments
Unbeamed control	7.96	NA	
1 e-beam pulse	8.75	9.9	9.65 GPa peak hardness at 2 μm deep
8 e-beam pulses	8.86	11.1	9.40 GPa peak hardness at 5 μm deep
1 e-beam pulse + cryogenic treatment	9.39	18.0	9.57 GPa peak hardness at 2 μm deep
8 e-beam pulses + cryogenic treatment	10.84	36.1	

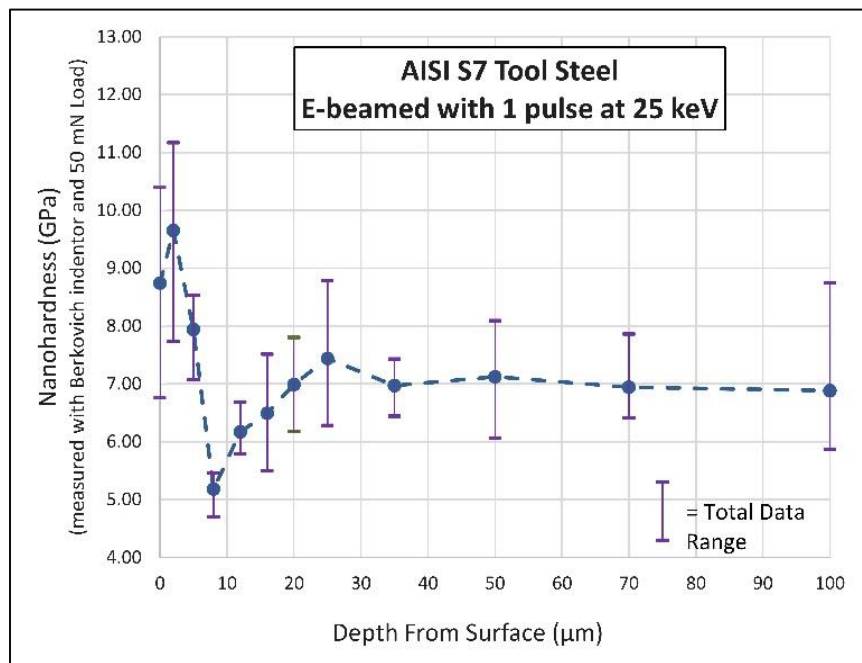


Figure 40. Nanohardness vs. depth after 1 e-beam pulse

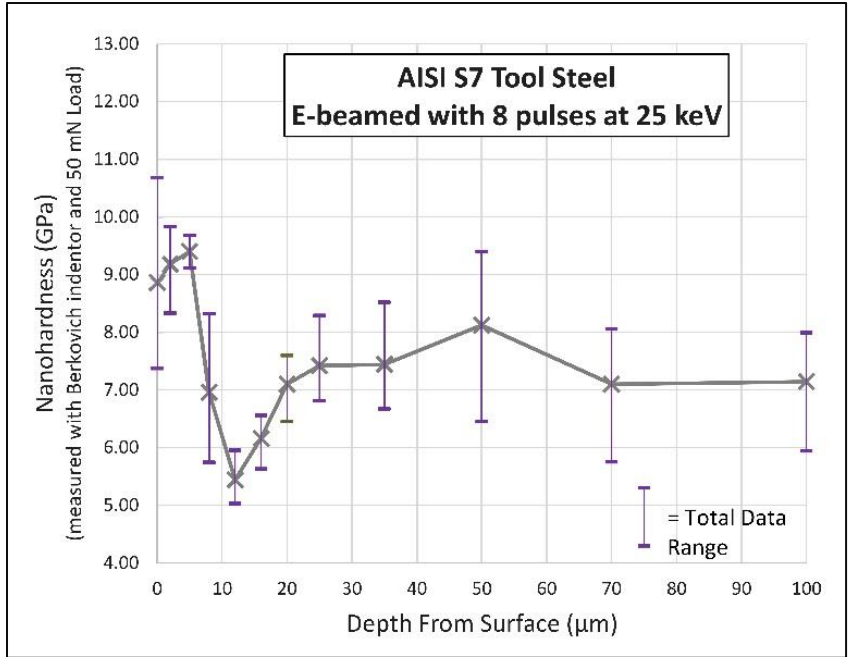


Figure 41. Nanoindentation hardness vs. depth after 8 e-beam pulses

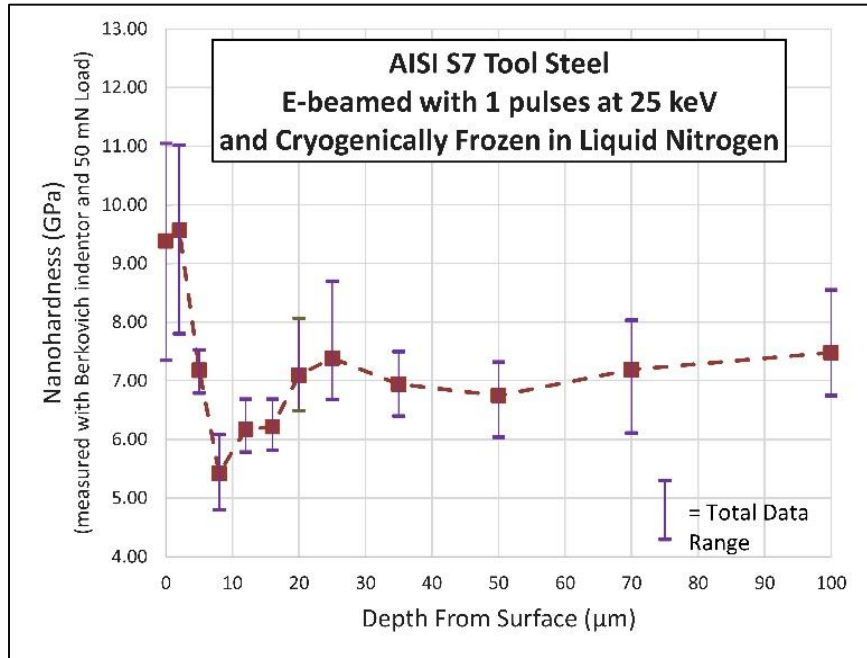


Figure 42. Nanoindentation hardness vs. depth after 1 e-beam pulse plus cryogenic treatment

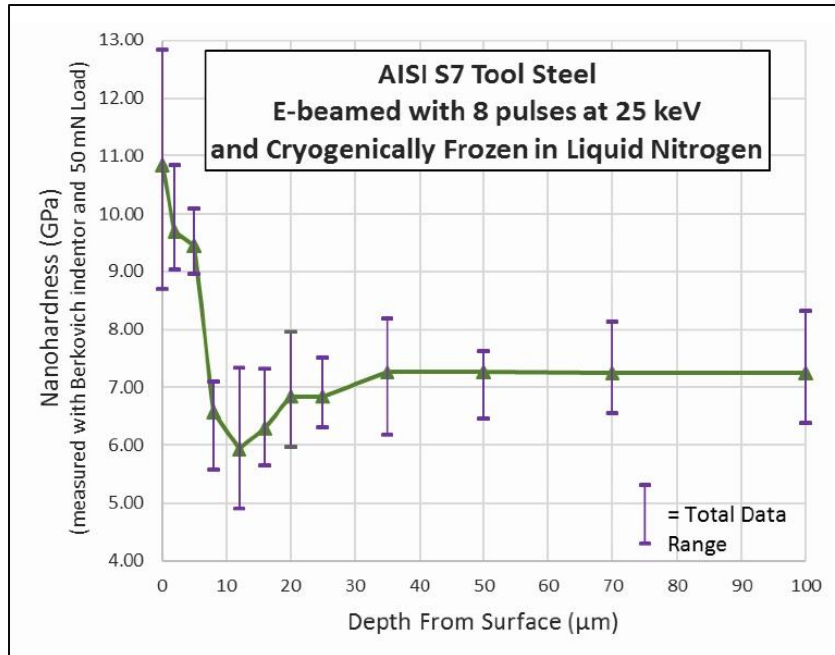


Figure 43. Nanohardness vs. depth after 8 e-beam pulses plus cryogenic treatment

All the e-beamed samples experienced a layer under the surface with reduced hardness corresponding to highly tempered martensite in a heat-affected zone. This area, which is highlighted in Figure 44, did not melt, but being adjacent to the melt, received enough heat to reach tempering temperatures. For some applications, the soft layer may pay dividends with an ability to yield and blunt a crack that forms in the hard case. In other applications, this softer underlying layer may be deleterious because yielding may cause an undesirable change in dimension.

The nanohardness profiles do not show any layers of clearly increased hardness beyond the heat-affected zones. Other studies have found clearly visible hardness peaks in layers deeper than the heat-affected zone and attributed them to work hardening by shock

waves.[8][9] The beam energy level used in this work may not have been sufficient to create this effect.

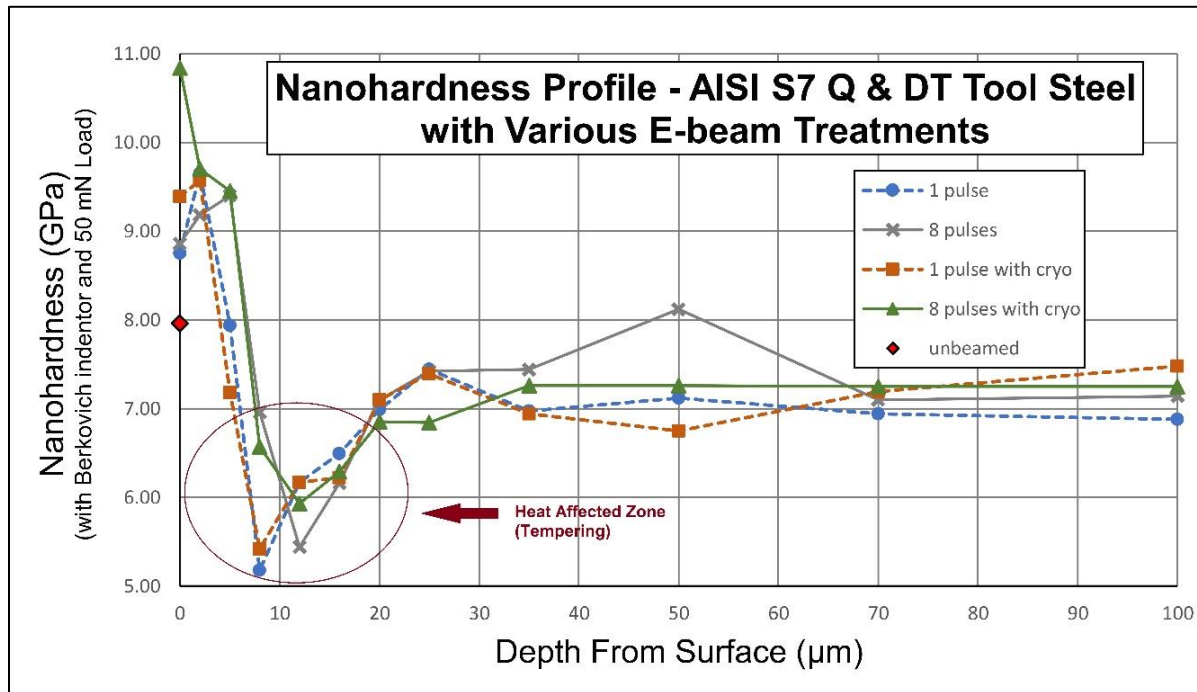


Figure 44. Nanohardness profile comparison of various e-beamed surface treatments

4.4. Grain Size

Figure 45 shows an AFM scan of a sample that received one e-beam pulse and was subsequently electropolished to a depth of 2 µm. A sample nanoindentation from the Berkovich indenter is also seen in Figure 45. The 2 µm depth from the original surface is within the significantly hardened layer. The grains or sub-grains which appear exhibit a size range of 100-300 nm which is in the UF grain size we defined and sought.

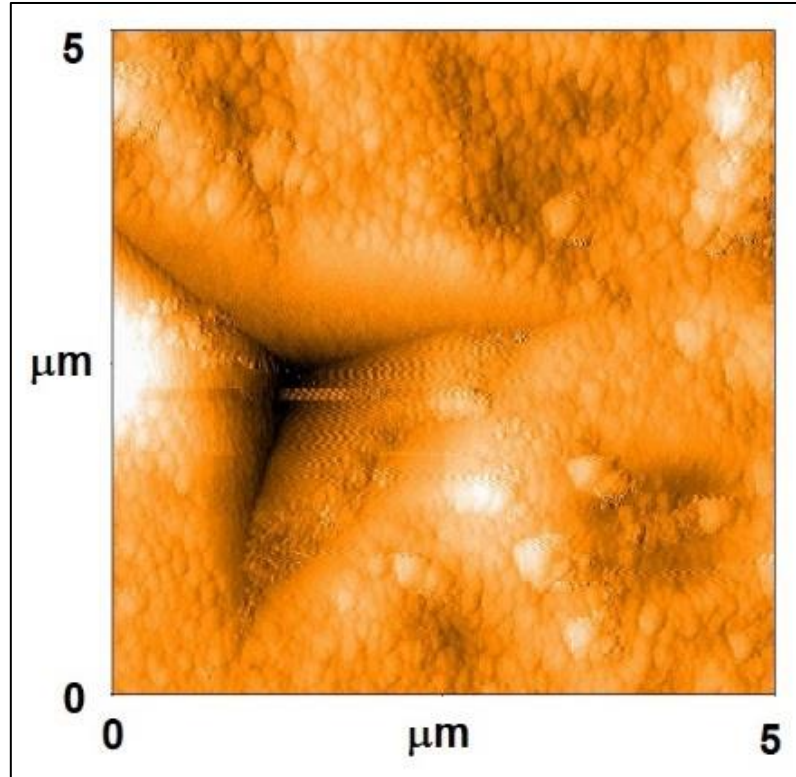


Figure 45. AFM of sample with nanoindentation after electropolishing to 2 μm depth

As presented in section 4.3, nanohardness profiles in Figure 40 - Figure 43 show clear surface hardening on all e-beamed samples. A significant contribution to the extra hardness is ascribed to Hall-Petch hardening due to the UF grain size of 100-300 nm as shown in the AFM image of Figure 45. The extremely rapid cooling rates discussed in section 2.3 result in significantly undercooled conditions which drives the generation of many more nucleation events than would occur with a normal industrial solidification process. With plentiful nucleation events occurring, the grains cannot grow far since they encounter other growing grains, which significantly limits average grain size. According to the well-known Hall-

Petch relationship discussed in section 2.4, grain boundaries and sub-grain boundaries act to strengthen and harden most metals.[46][47]

However, the combination of 8 pulses of e-beaming plus cryogenic freezing does show significantly higher hardness in Figure 43 and Figure 44 than the other treatments achieved. The result appears to be linked to the cryogenic freezing, since the sample with 8 pulses and no freezing in Figure 41 did not harden to the same extent.

4.5. Coefficient of Friction

The results from the dynamic coefficient of friction tests are summarized in Table 4. The Bruker testing device continuously and simultaneously monitored the z direction force and the x direction force while dragging a tungsten carbide ball on the surface. The device's software calculated instantaneous dynamic coefficient of friction from the two monitored forces. Very little differentiation in friction coefficient can be noticed among the surfaces. The output graphs for dynamic coefficient of friction are shown in Figure 46 through Figure 50. The unbeamed sample did show a noticeable trend of increasing friction as can be seen in Figure 46. Perhaps this sample was experiencing wear, as it is the softest of the samples. A subtler increase in friction over time may be seen in Figure 50 which shows the results for the sample which received 8 e-beam pulses as well as cryogenic treatment. The sample receiving 8 e-beam pulses plus cryogenic treatment was the hardest sample, so perhaps the coefficient of friction increase was indicative of brittle breakdown beginning on the surface. The instantaneous spikes on the graphs correspond to the change in direction of the slider. The spikes did not contribute appreciably to the average coefficient of friction because the

duration is very short and because the spikes at opposite ends of the travel were generally in opposite directions.

Table 4. Dynamic coefficient of friction test results: tungsten carbide ball on variously treated S7 steel surfaces

Sample	Average Coefficient of Friction	Observation
Unbeamed control	.145	Noticeable trend of increasing friction, possibly due to wear
1 e-beam pulse	.146	
8 e-beam pulses	.133	
1 e-beam pulse + cryogenic treatment	.135	
8 e-beam pulses + cryogenic treatment	.144	Subtle trend upward

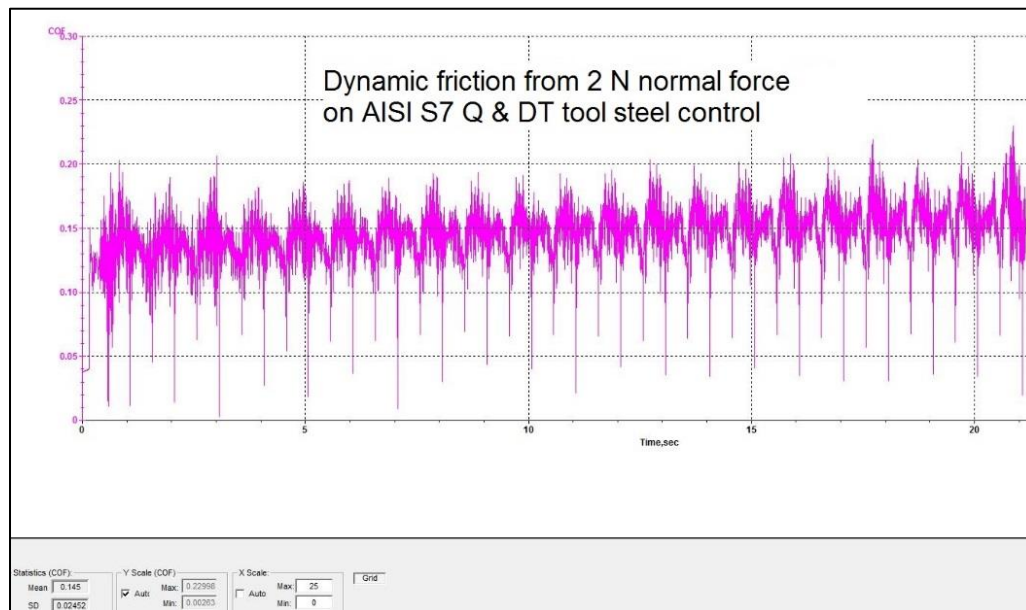


Figure 46. Coefficient of friction test for WC ball and unbeamed control sample

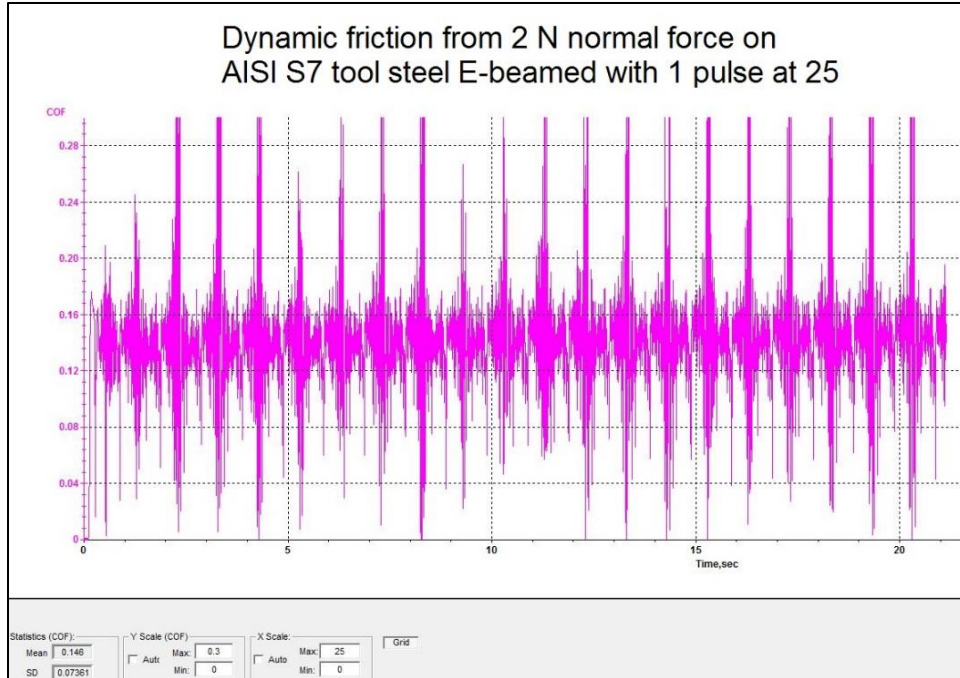


Figure 47. Coefficient of friction test for WC ball and sample e-beamed with 1 pulse

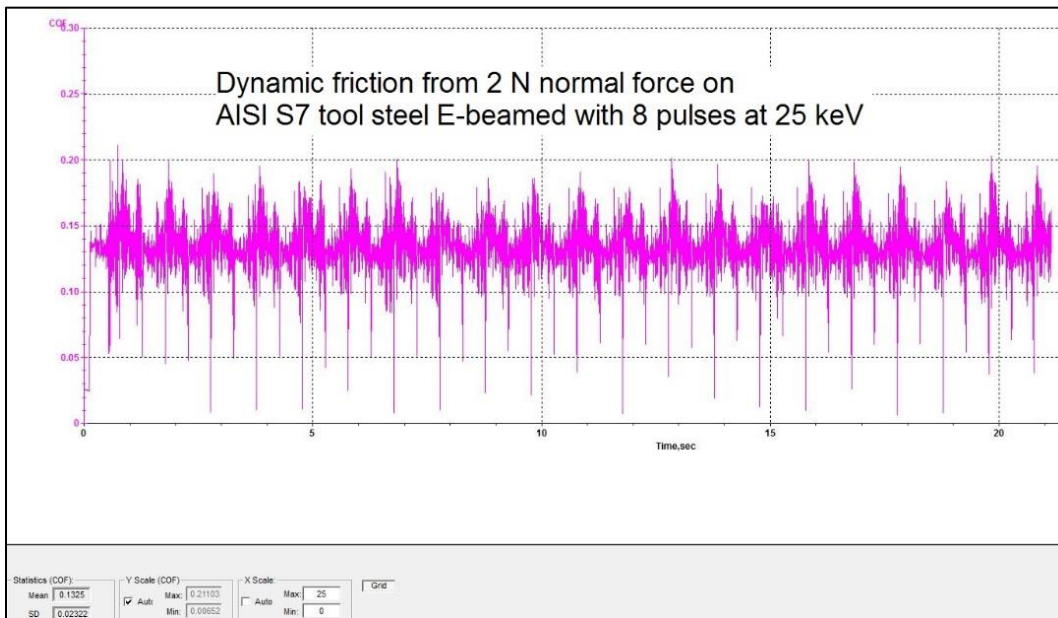


Figure 48. Coefficient of friction test for WC ball and sample e-beamed with 8 pulses

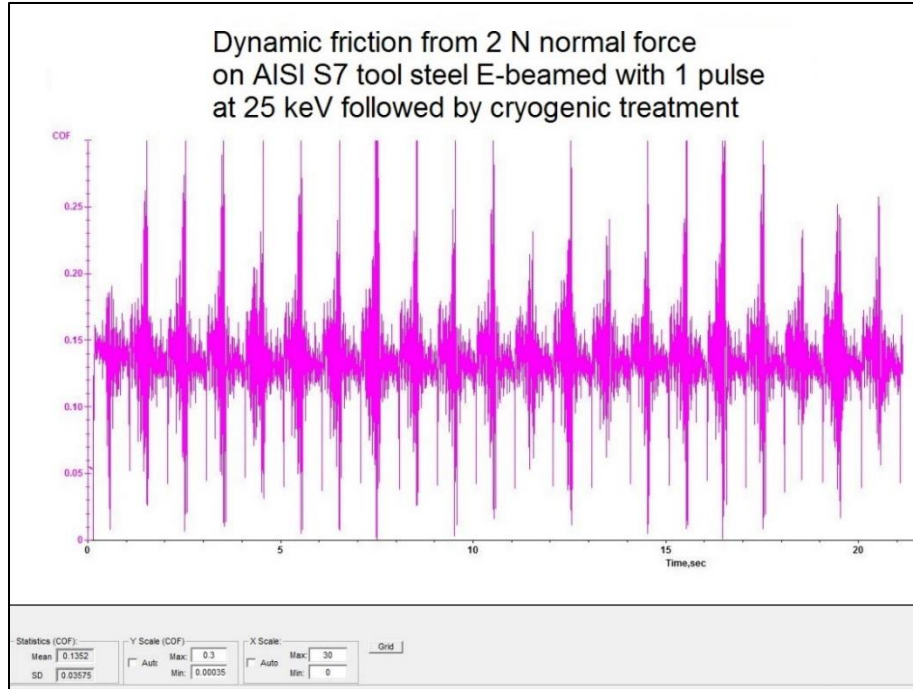


Figure 49. Coefficient of friction test for WC ball and sample e-beamed with 1 pulse and cryogenically treated



Figure 50. Coefficient of friction test for WC ball and sample e-beamed with 8 pulses and cryogenically treated

5. POTENTIAL FOR FUTURE WORK

As discussed in section 4.3, the combination of 8 pulses of e-beaming plus cryogenic freezing does show significantly higher hardness than the other treatments achieved. Further experimental work could be expended to determine and document the cause of this synergistic increase in hardening. Possible topics to investigate include differences in martensite morphology and the precipitation of η carbides which have both been found in conventionally heat treated tool steels which received cryogenic treatment.[86][87][88][89]

Section 4.3 also revealed the existence of a soft, tempered layer under the hard e-beamed layer. A benefit to overall performance may be found if the strength and hardness of this layer could be bolstered to better support the hard surface layer. Perhaps the tempered layer could be re-hardened by processing with a targeted loading to cause the layer to yield. The tempered layer, being softest, would yield first causing work hardening in the needed zone.

The results of section 3.6 showed that increasing the number of pulses increased the attainable hardness and the depth of elevated hardness. This work did not examine the application of pulse counts greater than 8. Further testing at increased pulse counts seems warranted.

In section 2.3 it was stated that the intensity and duration of the beam pulse affect melt depth. Although the present equipment has a fixed duration pulse, various other parameters can be adjusted to effect beam intensity. A study of the effect of increased beam intensity on layer depth and properties would be of interest.

6. CONCLUSIONS

The study of e-beamed S7 tool steel surface layers has yielded some important conclusions:

1. E-beam treatment of S7 tool steel creates elevated surface hardness due to the creation of ultrafine grain size in a melted and rapidly quenched surface layer.
2. Residual tensile stress is created within the e-beamed layer due to uneven contractions produced by dynamic heating, melting, and cooling.
3. Elevated quantities of metastable retained austenite have been found in the e-beamed layer.
4. Cryogenic freezing can produce significant reductions in the e-beamed layer's residual tensile stress, presumably due to transformation of the retained austenite into less-dense martensite.
5. Under some e-beam processing conditions, compressive stress can be created on the specimen's surface. Evaporative cooling enhanced by the low-pressure atmosphere in the e-beam device likely allows surface solidification before the full melt solidifies.
6. Due to the reduction in residual tensile stress, e-beamed and cryogenically treated tool steel surface layers are likely to be useful in more applications than surfaces receiving e-beaming treatment alone.

7. REFERENCES

- [1] D. A. College and Y. Zhu, “Alleviating surface tensile stress in e-beam treated tool steels by cryogenic treatment,” *Mater. Sci. Eng. A*, vol. 722, pp. 167–172, Apr. 2018.
- [2] D. I. Proskurovsky, V. P. Rotshtein, G. E. Ozur, Y. F. Ivanov, and A. B. Markov, “Physical foundations for surface treatment of materials with low energy, high current electron beams,” *Surf. Coatings Technol.*, vol. 125, no. 1–3, pp. 49–56, 2000.
- [3] K. M. Zhang, J. X. Zou, B. Bolle, and T. Grosdidier, “Evolution of residual stress states in surface layers of an AISI D2 steel treated by low energy high current pulsed electron beam,” *Vacuum*, vol. 87, pp. 60–68, Jan. 2013.
- [4] V. Surla and D. Ruzic, “High-energy density beams and plasmas for micro- and nano-texturing of surfaces by rapid melting and solidification,” *J. Phys. D. Appl. Phys.*, vol. 44, no. 17, p. 174026, 2011.
- [5] G. A. Roberts, R. Kennedy, and G. Krauss, *Tool Steels, 5th Edition*: ASM International, 1998.
- [6] C. W. White and M. J. Aziz, “Energy deposition, heat flow, and rapid solidification during pulsed-laser and electron-beam irradiation on materials,” in *Surface alloying by ion, electron, and laser beams: papers presented at the 1985 ASM Materials Science Seminar, 12-13 October 1985, Toronto, Ontario, Canada*, L. E. Rehn, S. T. Picraux, and H. Wiedersich, Eds. ASM, 1987.
- [7] J. W. Mayer, L. Eriksson, and J. A. Davies, *Ion Implantation in Semiconductors*. New York: Academic Press, 1970.

- [8] V. P. Rotshtein, "Metallic materials processing with intense pulsed electron beams," in *Proceedings of 12th International Conference on High-Power Particle Beams. BEAMS'98.*, M. Markovits and J. Shiloh, Eds. IEEE (Cat. No.98EX103), 1998, pp. 105–110.
- [9] A. N. Valyaev, A. D. Pogrebnyak, V. I. Lavrent'ev, S. N. Volkov, and S. V. Plotnikov, "Influence of the shock wave pressure gradient in α -Fe irradiated by a high-power ion beam on the occurrence of a microhardness maximum at large depths," *Tech. Phys. Lett.*, vol. 24, no. 2, pp. 9–11, 1998.
- [10] J. R. Davis, *Surface Hardening of Steels: Understanding the Basics*. ASM International, 2002.
- [11] D. M. Follstaedt and S. T. Picraux, "Microstructures of surface-melted alloys," in *Surface alloying by ion, electron, and laser beams : papers presented at the 1985 ASM Materials Science Seminar, 12-13 October 1985, Toronto, Ontario, Canada*, L. E. Rehn, S. T. Picraux, and H. Wiedersich, Eds. ASM, 1987, p. 417.
- [12] D. I. Proskurovsky, V. P. Rotshtein, and G. E. Ozur, "Use of low-energy, high-current electron beams for surface treatment of materials," *Surf. Coatings Technol.*, vol. 96, pp. 117–122, 1997.
- [13] D. I. Proskurovsky, V. P. Rotshtein, G. E. Ozur, A. B. Markov, and D. S. Nazarov, "Pulsed electron-beam technology for surface modification of metallic materials," *J. Vac. Sci. Technol.*, vol. 16, no. 4, p. 2480, 1998.

- [14] J. H. Lee, J. H. Jang, B. D. Joo, Y. M. Son, and Y. H. Moon, "Laser surface hardening of AISI H13 tool steel," *Trans. Nonferrous Met. Soc. China (English Ed.)*, vol. 19, no. 4, pp. 917–920, Aug. 2009.
- [15] R. Fetzer, G. Mueller, W. An, and A. Weisenburger, "Metal surface layers after pulsed electron beam treatment," *Surf. Coatings Technol.*, vol. 258, pp. 549–556, Nov. 2014.
- [16] J. Zou, K. Zhang, T. Grosdidier, and C. Dong, "Analysis of the evaporation and recondensation processes induced by pulsed beam treatments," *Int. J. Heat Mass Transf.*, vol. 64, pp. 1172–1182, 2013.
- [17] Y. F. F. Ivanov *et al.*, "Modification of steel surface layer by electron beam treatment," *Met. Sci. Heat Treat.*, vol. 50, no. 11–12, pp. 569–574, Nov. 2009.
- [18] K. Zhang, J. Zou, T. Grosdidier, and C. Dong, "Microstructure and property modifications of an AISI H13 (4Cr5MoSiV) steel induced by pulsed electron beam treatment," *J. Vac. Sci. Technol. A Vacuum, Surfaces, Film.*, vol. 28, no. 6, p. 1349, 2010.
- [19] G. Tang, F. Xu, G. Fan, X. Ma, and L. Wang, "Mechanisms of microstructure formations in M50 steel melted layer by high current pulsed electron beam," *Nucl. Instruments Methods Phys. Res. Sect. B Beam Interact. with Mater. Atoms*, vol. 288, pp. 1–5, Oct. 2012.
- [20] F. Xu *et al.*, "Microstructure modifications and corrosion behaviors of Cr4Mo4V steel treated by high current pulsed electron beam," *Mater. Chem. Phys.*, vol. 126, no. 3, pp. 904–908, Apr. 2011.

- [21] F. Xu, G. Tang, G. Guo, X. Ma, and G. E. Ozur, "Influence of irradiation number of high current pulsed electron beam on the structure and properties of M50 steel," *Nucl. Instruments Methods Phys. Res. Sect. B Beam Interact. with Mater. Atoms*, vol. 268, no. 15, pp. 2395–2399, Aug. 2010.
- [22] C.-C. Wang and J.-R. Hwang, "Surface hardening of AISI 4340 steel by electron beam treatment," *Surf. Coat. Technol.*, vol. 64, no. 1, pp. 29–33, 1994.
- [23] K. Zhang, J. Zou, T. Grosdidier, and C. Dong, "Crater-formation-induced metastable structure in an AISI D2 steel treated with a pulsed electron beam," in *Vacuum*, 2012, vol. 86, no. 9, pp. 1273–1277.
- [24] R. G. Song, K. Zhang, and G. N. Chen, "Electron beam surface treatment. Part I: surface hardening of AISI D3 tool steel," *Vacuum*, vol. 69, no. 4, pp. 513–516, 2003.
- [25] R. G. Song, K. Zhang, and G. N. Chen, "Electron beam surface remelting of AISI D2 cold-worked die steel," *Surf. Coatings Technol.*, vol. 157, no. 1, pp. 1–4, 2002.
- [26] J. X. Zou, T. Grosdidier, K. M. Zhang, B. Gao, S. Z. Hao, and C. Dong, "Microstructures and phase formations in the surface layer of an AISI D2 steel treated with pulsed electron beam," *J. Alloys Compd.*, vol. 434–435, no. SPEC. ISS., pp. 707–709, 2007.
- [27] J. X. Zou, T. Grosdidier, K. M. Zhang, and C. Dong, "Cross-sectional analysis of the graded microstructure in an AISI D2-steel treated with low energy high-current pulsed electron beam," *Appl. Surf. Sci.*, vol. 255, no. 9, pp. 4758–4764, 2009.

- [28] J. Zou, T. Grosdidier, K. Zhang, and C. Dong, "Mechanisms of nanostructure and metastable phase formations in the surface melted layers of a HCPEB-treated D2 steel," *Acta Mater.*, vol. 54, no. 20, pp. 5409–5419, 2006.
- [29] S. Hao, H. Wang, and L. Zhao, "Surface modification of 40CrNiMo7 steel with high current pulsed electron beam treatment," *Nucl. Instruments Methods Phys. Res. Sect. B Beam Interact. with Mater. Atoms*, vol. 368, pp. 81–85, 2016.
- [30] C. Dong *et al.*, "Surface treatment by high current pulsed electron beam," *Surf. Coatings Technol.*, vol. 163–164, pp. 620–624, 2003.
- [31] J. X. Zou, T. Grosdidier, B. Bolle, K. M. Zhang, and C. Dong, "Texture and microstructure at the surface of an AISI D2 steel treated by high current pulsed electron beam," *Metall. Mater. Trans. A Phys. Metall. Mater. Sci.*, 2007.
- [32] K. M. Zhang, J. X. Zou, and T. Grosdidier, "Nanostructure Formations and Improvement in Corrosion Resistance of Steels by Means of Pulsed Electron Beam Surface Treatment," *J. Nanomater.*, vol. 2013, pp. 1–8, 2013.
- [33] Y. Ivanov, W. Matz, V. Rotshtein, R. Günzel, and N. Shevchenko, "Pulsed electron-beam melting of high-speed steel: structural phase transformations and wear resistance," *Surf. Coatings Technol.*, vol. 150, no. 2–3, pp. 188–198, Feb. 2002.
- [34] V. P. Rotshtein and V. A. Shulov, "Surface Modification and Alloying of Aluminum and Titanium Alloys with Low-Energy, High-Current Electron Beams," *J. Metall.*, vol. 2011, pp. 1–15, 2011.

- [35] J.-R. Hwang and C.-P. Fung, "Effect of electron beam surface hardening on fatigue crack growth rate in AISI 4340 steel," *Surf. Coat. Technol.*, vol. 80, no. 3, pp. 271–278, 1996.
- [36] G. Leggieri *et al.*, "Pulsed electron beam for silicon annealing," *Vacuum*, vol. 32, no. 1, pp. 9–10, 1982.
- [37] G. E. Ozur, D. I. Proskurovsky, V. P. Rotshtein, and A. B. Markov, "Production and Application of Low-Energy, High-Current Electron Beams," *Laser Part. Beams*, vol. 21, no. 2, pp. 157–174, 2003.
- [38] G. A. Mesyats and D. I. Proskurovsky, *Pulsed Electrical Discharge in Vacuum*. Berlin: Springer, 1989.
- [39] Y. Samih *et al.*, "Microstructure modifications and associated hardness and corrosion improvements in the AISI 420 martensitic stainless steel treated by high current pulsed electron beam (HCPEB)," *Surf. Coatings Technol.*, vol. 259, no. PC, pp. 737–745, 2014.
- [40] ASM International, *Binary Alloy Phase Diagrams*, 2nd ed. Materials Park, OH, 1990.
- [41] M. A. Meyers and K. K. Chawla, *Mechanical Behavior of Materials*, 2nd ed. New York, NY: Cambridge University Press, 2009.
- [42] P. Cavaliere, "Fatigue properties and crack behavior of ultra-fine and nanocrystalline pure metals," *Int. J. Fatigue*, vol. 31, no. 10, pp. 1476–1489, 2009.
- [43] T. Hanlon, E. D. Tabachnikova, and S. Suresh, "Fatigue behavior of nanocrystalline metals and alloys," *Int. J. Fatigue*, vol. 27, no. 10–12, pp. 1147–1158, 2005.

- [44] M. A. Meyers, A. Mishra, and D. J. Benson, "Mechanical properties of nanocrystalline materials," *Prog. Mater. Sci.*, vol. 51, no. 4, pp. 427–556, 2006.
- [45] G. S. Ansell, S. J. Donachie, and R. W. Messler, "The effect of quench rate on the martensitic transformation in Fe–C alloys," *Metall. Trans.*, vol. 2, no. 9, pp. 2443–2449, Sep. 1971.
- [46] E. O. Hall, "The deformation and ageing of mild steel III: Discussion of results," *Proc. Phys. Soc. Sect. B*, vol. 64, no. 9, p. 747, 1951.
- [47] N. J. Petch, "The cleavage strength of Polycrystals," *J. Iron Steel Inst.*, vol. 174, pp. 25–28, 1953.
- [48] D. G. Morris, "The origins of strengthening in nanostructured metals and alloys," *Rev. Metal.*, vol. 46, no. 2, pp. 173–186, 2010.
- [49] M. F. Ashby, "The deformation of plastically non-homogeneous materials," *Philos. Mag.*, vol. 21, no. 170, pp. 399–424, 1970.
- [50] A. H. Cottrell, "Theory of brittle fracture in steel and similar metals," *Trans. Metall. Soc. AIME*, vol. 212, 1958.
- [51] J. C. M. Li and Y. T. Chou, "The role of dislocations in the flow stress grain size relationships," *Metall. Mater. Trans. B*, vol. 1, no. 5, p. 1145, May 1970.
- [52] N. A. Fleck, G. M. Muller, M. F. Ashby, and J. W. Hutchinson, "Strain gradient plasticity: theory and experiment," *Acta Metall. Mater.*, vol. 42, no. 2, pp. 475–487, 1994.
- [53] M. A. Meyers and E. Ashworth, "A model for the effect of grain size on the yield stress of metals," *Philos. Mag. A*, vol. 46, no. August, pp. 737–759, 1982.

- [54] R. K. Guduru, R. O. Scattergood, C. C. Koch, K. L. Murty, S. Guruswamy, and M. K. McCarter, "Mechanical properties of nanocrystalline Fe-Pb and Fe-Al₂O₃," *Scr. Mater.*, vol. 54, no. 11, pp. 1879–1883, 2006.
- [55] C. Cheung, F. Djuanda, U. Erb, and G. Palumbo, "Electrodeposition of nanocrystalline Ni-Fe alloys," *Nanostructured Mater.*, vol. 5, no. 5, pp. 513–523, 1995.
- [56] C. Suryanarayana and A. Inoue, "Iron-based bulk metallic glasses," *Int. Mater. Rev.*, vol. 58, no. 3, pp. 131–166, 2013.
- [57] P. S. Prevéy, "X-ray diffraction residual stress techniques," in *Metals Handbook. Vol 10.*, 9th ed., K. Mills, Ed. Metals Park, OH: American Society for Metals, 1986, pp. 380–392.
- [58] H. P. Klug and L. E. Alexander, *X-Ray Diffraction Procedures for Polycrystalline and Amorphous Materials*, 2nd ed. New York: John Wiley and Sons, 1974.
- [59] M. Lee, *X-Ray Diffraction for Materials Research*. New York: Apple Academic Press, 2016.
- [60] ACTTR Technology, "StressX Residual Stress Analyzer XRD." [Online]. Available: <http://product.acttr.com/en/spectrometer-c-13/x-ray-spectrometer-c-74/stressx-residual-stress-analyzer-xrd-p-226>.
- [61] S. S. Gill, J. Singh, R. Singh, and H. Singh, "Metallurgical principles of cryogenically treated tool steels - A review on the current state of science," *Int. J. Adv. Manuf. Technol.*, 2011.
- [62] "ASTM A681 Standard Specification for Tool Steels Alloy." ASTM International, West Conshohocken, PA.

- [63] P. Pendyala, M. S. Bobji, and G. Madras, “Evolution of surface roughness during electropolishing,” *Tribol. Lett.*, vol. 55, no. 1, pp. 93–101, 2014.
- [64] P. J. Núñez, E. García-Plaza, M. Hernando, and R. Trujillo, “Characterization of surface finish of electropolished stainless steel AISI 316L with varying electrolyte concentrations,” *Procedia Eng.*, vol. 63, pp. 771–778, 2013.
- [65] G. Yang, B. Wang, K. Tawfiq, H. Wei, S. Zhou, and G. Chen, “Electropolishing of surfaces: theory and applications,” *Surf. Eng.*, vol. 33, no. 2, pp. 149–166, 2017.
- [66] R. Jenkins and R. L. Snyder, *Introduction to X-ray Powder Diffraction*. New York: John Wiley & Sons, 1996.
- [67] B. D. Cullity and S. R. Stock, *Elements of X-ray Diffraction*, 3rd ed. New York: Prentice-Hall, 2001.
- [68] M. E. Fitzpatrick, A. T. Fry, P. Holdway, F. A. Kandil, J. Shackleton, and L. Suominen, “Determination of Residual Stresses by X-ray Diffraction - Issue 2,” A *National Measurement Good Practice Guide No. 52*. National Physical Laboratory, Teddington, United Kingdom, 2005.
- [69] E. Zolotoyabko, *Basic Concepts of X-Ray Diffraction*. Weinheim, GERMANY: John Wiley & Sons, Incorporated, 2014.
- [70] S. Talebi, H. Ghasemi-Nanesa, M. Jahazi, and H. Melkonyan, “In Situ Study of Phase Transformations during Non-Isothermal Tempering of Bainitic and Martensitic Microstructures,” *Metals (Basel)*, vol. 7, no. 9, p. 346, 2017.

- [71] “ASTM E975-13 Standard Practice for X-Ray Determination of Retained Austenite in Steel with Near Random Crystallographic Orientation.” ASTM International, West Conshohocken, PA, 2013.
- [72] I. C. Noyan and J. B. Cohen, *Residual Stress: Measurement by Diffraction and Interpretation*. New York: Springer, 1987.
- [73] SAE Iron and Steel Technical Committee, *Residual Stress Measurement by X-ray Diffraction - SAE J784a*. Society of Automotive Engineers, 1971.
- [74] *Residual Stress Measurement by X-ray Diffraction: HS-784*. SAE International, 2003.
- [75] D. Newey, M. A. Wilkins, and H. M. Pollock, “An ultra-low-load penetration hardness tester,” *J. Phys. E.*, vol. 15, no. 1, pp. 119–122, 1982.
- [76] ASTM International, “ASTM E10-17 Standard Test Method for Brinell Hardness of Metallic Materials.” ASTM International, West Conshohocken, PA, 2017.
- [77] ASTM International, “ASTM E18-17e1 Standard Test Methods for Rockwell Hardness of Metallic Materials.” ASTM International, West Conshohocken, PA, pp. 1–38, 2017.
- [78] ASTM International, “E384 -17 Standard Test Method for Microindentation Hardness of Materials.” ASTM International, West Conshohocken, PA, 2017.
- [79] O. Sahin, O. Uzun, M. Sopicka-Lizer, H. Gocmez, and U. Kölemen, “Analysis of load-penetration depth data using Oliver-Pharr and Cheng-Cheng methods of SiAlON-ZrO₂ ceramics,” *J. Phys. D. Appl. Phys.*, vol. 41, no. 3, 2008.

- [80] W. C. Oliver and G. M. Pharr, "Measurement of hardness and elastic modulus by instrumented indentation: Advances in understanding and refinements to methodology," *J. Mater. Res.*, vol. 19, no. 1, pp. 3–20, Jan. 2004.
- [81] J. B. Pethica, R. Hutchings, and W. C. Oliver, "Hardness measurement at penetration depths as small as 20 nm," *Philos. Mag. A Phys. Condens. Matter, Struct. Defects Mech. Prop.*, vol. 48, no. 4, pp. 593–606, 1983.
- [82] E. S. Berkovich, "Three-faceted diamond pyramid for micro-hardness testing," *Ind. Diam. Rev.*, vol. 11, 1951.
- [83] A. C. Fischer-Cripps, *Nanoindentation*. New York: Springer-Verlag, 2004.
- [84] J. M. Wheeler, R. A. Oliver, and T. W. Clyne, "AFM observation of diamond indenters after oxidation at elevated temperatures," *Diam. Relat. Mater.*, vol. 19, no. 11, pp. 1348–1353, 2010.
- [85] S. Shaffer, S. Kuiry, and J. Earle, "Universal Mechanical Testers for Tribology Testing in the Automotive Industry," *NASA Tech Briefs*, Sep-2014.
- [86] A. Oppenkowski, S. Weber, and W. Theisen, "Evaluation of factors influencing deep cryogenic treatment that affect the properties of tool steels," *J. Mater. Process. Technol.*, vol. 210, no. 14, pp. 1949–1955, 2010.
- [87] H. Li, W. Tong, J. Cui, H. Zhang, L. Chen, and L. Zuo, "The influence of deep cryogenic treatment on the properties of high-vanadium alloy steel," *Mater. Sci. Eng. A*, vol. 662, 2016.

- [88] V. G. Gavriljuk *et al.*, “Low-temperature martensitic transformation in tool steels in relation to their deep cryogenic treatment,” *Acta Mater.*, vol. 61, no. 5, pp. 1705–1715, 2013.
- [89] J. Sobotova, P. Jurci, and I. Dlouhy, “The effect of subzero treatment on microstructure, fracture toughness, and wear resistance of Vanadis 6 tool steel,” *Mater. Sci. Eng. A*, vol. 652, pp. 192–204, 2016.